

Contents lists available at ScienceDirect

Solar Energy

journal homepage: www.elsevier.com/locate/solener





Effects of concentrated solar–integrated packed-bed thermal energy storage operation on solid oxide electrolysis cell performance[★]

Timo Roeder ^{a,c,*}, Yasuki Kadohiro ^a, Kai Risthaus ^b, Anika Weber ^{b,c}, Enric Prats-Salvado ^{a,c}, Nathalie Monnerie ^a, Christian Sattler ^{a,c}

- a Deutsches Zentrum für Luft- und Raumfahrt DLR/German Aerospace Center, Institute of Future Fuels, Linder Höhe, 51147 Cologne, Germany
- b Deutsches Zentrum für Luft- und Raumfahrt DLR/German Aerospace Center, Institute of Future Fuels, Im Langenbroich 13, 52428 Jülich, Germany
- c RWTH Aachen University, Faculty of Mechanical Engineering, Chair of Solar Fuel Production, 52062 Aachen, Germany

ARTICLE INFO

Keywords: Solar energy Packed bed thermal energy storage Experimental and numerical analysis High-temperature electrolysis Green hydrogen Particles

ABSTRACT

The use of renewable energy in the context of green hydrogen production requires suitable energy storage technologies to compensate for intermittent wind and solar resources. High-temperature electrolysis is a promising way to produce hydrogen as it has the highest electrical efficiency by using steam instead of liquid water compared to low temperature electrolysis. Here, a part of the total energy demand is substituted by thermal energy. For a sustainable and continuous process operation with concentrated solar energy, a high-temperature thermal energy storage heating air and steam is required to operate the high-temperature electrolysis above 800 °C. In this study, the charging and discharging behavior of a packed bed thermal energy storage with a capacity of 17.46 kWh is experimentally tested and a utility scale storage numerically analyzed. The storage is charged with superheated steam from a solar cavity receiver and discharged with ambient air or steam flow. The storage discharge temperature profile results in a change in the electrolysis operating state and therefore, a change in the reagent flow rate. This changes the hydrogen production capacity during the discharge period. Adjusting the thermal energy storage discharge flow rate maintains an electrical conversion efficiency of 97 %. Furthermore, additional electric heating or exothermal operation of the electrolysis is avoided. Additionally, an electrolysis cooling rate of greater than -0.3 K/min can be maintained.

1. Introduction

As part of the European Green Deal, hydrogen will be a cornerstone to become climate neutral [1]. Green hydrogen production by high-temperature electrolysis (HTE) using electricity and heat is expected to cover a significant amount of the future hydrogen supply [2]. HTE combined with concentrated solar energy to superheat water and air to temperatures up to 800 °C can reduce the specific electrical energy demand of the HTE significantly compared to low temperature electrolysis technologies [3,4]. Note that both high-temperature steam and air are necessary for the electrolysis operation: Steam is needed to split it into hydrogen and oxygen, and air is needed to a) maintain a low oxygen partial pressure at the air electrode of the electrolysis [5] and b) for thermal management [6]. For lowest hydrogen production cost, high annual operating full load hours (i.e. beyond a daytime operation) are required [7]. To achieve this high operation time, an energy storage for

steam and air heating must be used to supply heat continuously despite the inherent intermittence of solar energy.

Previous studies mainly focused on low-temperature thermal energy storage for steam generation. In this case, the steam has to be superheated electrically [8–17]. So, integrating high-temperature storage here can increase the electrical efficiency. However, storing steam directly in a steam accumulator is inefficient [18] and only suitable for short transients [19,20]. Consequently, one storage for heating air and another storage for water evaporation and superheating is needed. Buffer storages can be integrated in the HTE directly, but for bridging a night, external storages are required. Several options exist for such storages. The use of aluminum alloys [21,22] as latent or cobalt-oxide [23] as thermochemical energy storage is applicable for the operating temperatures of a HTE. Hosseinpour et al. [24] and Hwang et al. [25] considered the use of particle bed thermocline storage showing an increase in round-trip-efficiency and cost reduction potential for a reversible solid oxide cell operation. However, the use of a thermocline

E-mail address: timo.roeder@dlr.de (T. Roeder).

 $^{^{\}star}$ This article is part of a special issue entitled: 'Solar-to-X' published in Solar Energy.

^{*} Corresponding author.

Naman	-lat	L	Storage height m	
Nomenclature		M	Molar mass g mol ⁻¹	
Abbreviation Full Description		m ivi	Mass flow rate kg s ⁻¹	
	Direct Normal Irradiation		Nusselt number —	
DNI FR	Flow Recorder	Nu	Nusselt number between particle bed and the wall –	
FRC	Flow Recorder & Controller	Nu _W n	Molar flow rate mol s ⁻¹	
FS	Full Scale		Cell power W	
rs HTE	High-Temperature Electrolysis	P _{cell} Pr	Prandtl number –	
	F97 International Association for the Properties of Water	p p	Pressure bar	
IAP WS-I	and Steam		₂₀ , p ₀₂ Partial pressure of hydrogen, steam or oxygen,	
T T T T 7	Lower heating value of hydrogen (33.33 kWh kg ⁻¹)	PH2, PH2	respectively bar	
LHV PR	Pressure Recorder	ċ		
Rd		Q O	Thermal Power W	
	Reading value	Q_{TES}	Storage capacity Wh	
SOC TES	State of Charge Thermal Energy Storage	R D-	Universal gas constant ($R = 8.314462618$) J K^{-1} mol ⁻¹	
TR	Temperature Recorder	Re	Reynolds number $-$ Volume specific surface area m ² m ⁻³	
	ymbols Full Description Units	$rac{S_{ m v}}{T}$		
α	Heat transfer coefficient W m ⁻² K ⁻¹		Temperature K or °C	
β	Mass overrating factor –	T_{ref}	Reference temperature for the area specific resistance calculation K	
δ	Specific exponent to calculate the volumetric heat transfer	T	Absolute temperature K or °C	
O	coefficient –	T T	-	
ε	Emissivity –		Weighted mean temperature K or °C	
θ	Rated hydrogen production rate –	Ť	Temporal temperature gradient K min ⁻¹	
λ	Thermal conductivity W m ⁻¹ K ⁻¹	t _{TES}	Storage discharge duration h	
μ	Dynamic viscosity Pa s	U	Thermal transmittance coefficient W m ⁻² K ⁻¹	
ρ	Density kg m ⁻³	U_{cell}	Cell voltage V	
Ψ	Porosity –	U_{ideal}	Ideal cell voltage V	
η	Efficiency %	U _{tn}	Thermoneutral voltage V Velocity m s $^{-1}$	
	mbols Full Description Units	u V	Velocity m s Volume m ³	
A	Cross sectional Area m ²			
AR	Aspect ratio –		ipts Full Description Ambient conditions	
ASR	Area specific resistance Ω cm ⁻²	amb bed	Particle bed	
ASR_0	Area specific resistance factor Ωcm^{-2}	cap	Capacity	
C _p	Specific heat capacity kJ kg ⁻¹ K ⁻¹	cap	Electrolysis cell	
C _f	Particle shape factor –	eff	Effective	
D D	Storage diameter m		Gas phase	
d_p	Particle diameter m	g i	Index for the number of insulation layers	
$\frac{d_p}{d_p}$	Sauter diameter m	in	Inner surface	
	Insulation thickness m	ins	Insulation	
d _{ins} F	Faraday constant C mol ⁻¹	nom	Nominal conditions	
$f_1(Pr)$	Function of Pr for the calculation of the thermal	out	Outer surface	
11(11)	transmittance coefficient U –	p	Particle	
$h_{\rm v}$	Volumetric heat transfer coefficient W m ⁻³ K ⁻¹	S S	Solid phase	
j	Current density A cm ⁻²	-	· · · · · ·	
J	Current denoity It cin			

storage shows a transient temperature behavior during discharge if no active thermocline control method is applied [26,27]. Hwang et al. [25] investigated the electrolysis operation at constant current density resulting in an exothermal electrolysis operation during the discharge of the thermal energy storage (TES). However, the impact of a storage on the HTE operation at constant thermoneutral operation is to be investigated. Ideally, the TES is charged at higher temperature and the TES outlet stream is mixed with a colder stream [26,27] to achieve thermoneutral HTE temperatures. Alternatively, the HTE can be operated according to the TES outlet temperature to maintain thermoneutral operation conditions. The HTE is therefore operated in part load which results in high electrical energy conversion efficiencies [9]. Such a transient operation in combination with a thermocline storage has not been investigated, yet. Moreover, the integration strategy of the TES and the concentrated solar thermal system has to be identified.

In this study, a system with a direct steam generating and air heating cavity receiver [28–30] can directly provide the required HTE

temperatures for steam and air streams is considered. Neither a heat exchanger to transfer heat from another heat transfer medium nor an electric heater is required in here. The concentrating solar system can then be designed to provide a surplus of air or steam, or both, compared to the nominal load in order to charge the storages. Nonetheless, due to the higher volumetric heat capacity compared to air, steam is a better heat transfer media. Moreover, the exergy demand to charge a thermal energy storage can be significantly reduced because water as a liquid, which is then evaporated and superheated, requires less energy to pump than air as a gas. In addition, Edwards and Bindra [31] found a higher exergetic efficiency of a TES by using steam and storing the heat of condensation in comparison to air as heat transfer media. Furthermore, steam is not limited by the operating temperature like the typically used molten salt or thermal oil [32,33]. Last but not least, steam can also be used as a reducing atmosphere for redox reactions: Instead of inert storage material, redox reactive materials can be utilized increasing the storage capacity by a thermochemical redox reaction [34–36].

The objective of this study is to show the coupling of a single solar cavity receiver producing high temperature steam and air simultaneously with an inert packed bed thermal energy storage using bauxite particle. Steam and air are used as heat transfer media for the charging and discharging of the TES, respectively. Therefore, an experimental setup is designed to produce steam and air at temperatures above 800 °C using concentrated light [28]. Steam at this elevated temperature is directly used to charge a packed bed thermocline storage. Thus, not only one component is analyzed individually but also the interaction of the receiver and the storage as an entire system. The results from the experimental test campaign are used to validate a numerical model to further analyze the storage impact on the electrolysis operation conditions and hydrogen production rate. In a HTE process, temporal temperature gradients at the inlet streams of the electrolysis cell should be as low as possible. This is because introducing a temperature gradient into the stack can lead to thermomechanical stresses and therefore to failure [37]. In terms of the TES design, a higher aspect ratio [38,39] shows an improved thermocline behaviour. Similarly, smaller particle diameters [40,41] can achieve the same effect. Different inert materials [41] or bed porosities [38,40] also impact the thermocline behaviour, but are causing a minor change. Using phase change or thermchemical reactive materials are also affecting the thermocline behavior [42–45], but are not further analysed here. In this study, only the material properties, particle diameter, and porosity matching to the experimental setup are considered. Hence, the temperature gradients during discharge are studied numerically for two different aspect ratios to identify suitable discharge and electrolysis operation strategies. Furthermore, the hydrogen production rate during the discharge is calculated. A design recommendation for the combination of a high-temperature packed bed TES in combination with a high-temperature electrolysis is given for an efficient hydrogen production.

2. Numerical model description and analysis methodology

A parametric study is needed to optimize the packed bed storage for a concentrated solar thermal powered HTE. For this parameter study, the influence of geometrical changes and the impact of a flow rate adjustment according to the electrolysis operating conditions is analyzed. Therefore, a numerical analysis is conducted for a cylindrical tank filled with particles. A previously used one dimensional two-phase model [46] based on a model by Schumann [47] is used to investigate the storage behavior using steam as a heat transfer medium during the charging and air during the discharging phase of the storage. In the present study, thermal losses are considered. The packed bed TES model consists therefore of an energy balance, Equation (1) for the heat transfer media and Equation (2) for the solid particle filler.

$$\rho_g \left(\psi c_{p,g} \frac{\partial T_g}{\partial t} + \psi u c_{p,g} \frac{\partial T_g}{\partial x} \right) = h_v \big(T_s - T_g \big) - \frac{U D \pi}{A} \big(T_g - T_{amb} \big) \tag{1} \label{eq:pg}$$

$$\rho_{s}(1-\psi)c_{p,s}\frac{\partial T_{s}}{\partial t}=\frac{\partial}{\partial x}\bigg(\lambda_{eff,s}\frac{\partial T_{s}}{\partial x}\bigg)-h_{v}\big(T_{s}-T_{g}\big) \tag{2} \label{eq:2}$$

In Equation (1) and (2), T is the temperature, ρ the density, c_p the specific heat capacity, h_v the volumetric heat transfer coefficient, $\lambda_{eff.s}$ the effective thermal conductivity of the bed, u the gas phase velocity, U the thermal transmittance through the insulation, ψ the average bed porosity, D the storage diameter and A its cross sectional area. The subscripts s and g stand for the solid and gas phase, respectively. Both equations are coupled by h_v to consider the heat exchange between the heat transfer media and the solid filler. In contrast to the previous study, a different model for calculating the volumetric heat transfer coefficient and for the pressure drop through fluid flow are used. Furthermore, temperature dependent properties for steam and air are considered. Details about the adaptions are explained in the following subsections.

2.1. Volumetric heat transfer coefficient

The correlation of Qi and Yu [48] is used to calculate h_v because other models show difficulties in estimating the Nusselt number (Nu) at low Reynolds numbers (Re). For example, the Gnielinski model overestimates Nu at low Re and especially at low Peclet numbers [49,50]. In contrast, the model by Qi and Yu has been validated over a wide range of Prandtl numbers (Pr) (0.1–10), Re (1–500), and bed porosity (ψ) (0.35–0.79) [48]. For the sake of completeness, the equations are repeated here. The Nu is calculated as the product of the particle Nusselt number Nu_p according to Equation (3)-(5) with a specific exponent δ based on the bed porosity, the dimensionless particle Reynolds and Prandtl numbers.

$$Nu = Nu_p (Re Pr)^{1-\psi} \psi^{-\delta}$$
 (3)

$$Nu_{p} = 2 + 0.478 Re^{0.48} Pr^{0.45} + 0.012 Re^{1.1} Pr^{0.78}$$
(4)

$$\begin{split} \delta &= \left(3.92\,\psi^2 + 0.34\,\psi + 10.3\right) - 12\,\text{exp}^{0.38\,\psi^2\,\text{log}_e(Pr)} \\ &+ \left(3.13\,\psi^3 - 5.43\,\psi^2\right)\text{log}_e(Re) \end{split} \tag{5}$$

Thus, h_v is calculated as

$$h_{v} = S_{v} Nu \frac{\lambda_{g}}{d_{n}}$$
 (6)

with the volume specific surface area $S_v=\frac{6(1-\psi)}{d_p}$ and the volume average particle diameter $d_p.$

2.2. Pressure drop through fluid flow

To account for the local pressure, the pressure drop Δp along the axial axis of a packed particle bed is calculated using the Ergun equation [51], see Equation (7). The pressure drop is influenced by the bed porosity $\psi,$ the dynamic viscosity $\mu,$ velocity u, and the density ρ_g of the heat transfer media. Additionally, a characteristic particle diameter $\overline{d}_p,$ also known as the Sauter diameter, is used. For spherical particles, this is $\overline{d}_p=6/S_\nu.$

$$\frac{\Delta p}{\Delta L} = 150 \; \frac{(1-\psi)^2}{\psi^3} \; \frac{\mu \, u}{\overline{d_p}^2} + 1.75 \; \frac{1-\psi}{\psi^3} \; \frac{\rho_g \, u^2}{\overline{d}_p} \tag{7} \label{eq:7}$$

2.3. Thermal losses

To store thermal energy efficiently, the storage unit is covered with insulating material. However, perfect insulation is not possible. Therefore, the thermal transmittance coefficient U is calculated based on the storage geometry, the diameter D_i of each insulation layer i, and the thermal conductivity of the insulation with Equation (8) [52]. The heat transfer inside and outside the storage is calculated with Equation (9)-(13) [49]. Equation (9) and (10) are used to calculate the heat transfer coefficient between the wall and the particle bed using the empty volume Reynolds number over a single particle $Re_0 = u\,d_p/\mu$ and the ratio between the effective bed and gas heat transfer coefficient λ_{bed}/λ_g calculated with the Zehner-Bauer-Schlünder model [53,54]. The heat transfer by natural convection at the outer shell surface of the storage is calculated from Equation (11)-(13) using the Rayleigh number (Ra) for free convection at a vertical plate.

$$\frac{1}{U} = \frac{1}{\alpha_{in}} + \frac{D}{2} \sum \frac{1}{\lambda_{i}} ln \frac{D_{i+1}}{D_{i}} + \frac{1}{\alpha_{out}} \frac{D}{D_{out}}$$
 (8)

$$\alpha_{in} = \frac{Nu_W \lambda_g}{d_n} \tag{9}$$

$$Nu_W = \left(1.3 + \frac{5}{D/d_p}\right) \frac{\lambda_{bed}}{\lambda_g} + 0.19 \, Re_0^{0.75} \, Pr^{1/3} \tag{10} \label{eq:NuW}$$

$$\alpha_{out} = \frac{Nu_{out} \lambda_g}{I} \tag{11}$$

$$Nu_{out} = \left\{ 0.825 + 0.387 \left[Ra \, f_1(Pr) \right]^{1/6} \right\}^2 \tag{12}$$

$$f_1(Pr) = \left\lceil 1 + \left(\frac{0.492}{Pr} \right)^{9/16} \right\rceil^{-16/9} \tag{13}$$

2.4. Thermophysical properties

Temperature and pressure dependent thermophysical properties of the heat transfer media air and steam are considered. For air, polynomial functions, Equation (14)-(16), are used to calculate the specific heat capacity c_p with the universal gas constant R and the molar mass M of air, the dynamic viscosity μ , and the thermal conductivity λ of air as a function of temperature with the coefficients from Table 1 [49]. Additionally, the density of air is calculated using the ideal gas law.

$$\begin{split} \frac{c_p}{J g^{-1} K^{-1}} &= \frac{R}{M} \left\{ B + (C - B) \left(\frac{T}{A + T} \right)^2 \left[1 - \frac{A}{A + T} \left(D + E \frac{T}{A + T} \right) + F \left(\frac{T}{A + T} \right)^2 + G \left(\frac{T}{A + T} \right)^3 \right) \right\} \end{split} \tag{14}$$

$$\frac{\lambda}{W\,m^{-1}\,K^{-1}}\!=\,A+B\,T+C\,T^2+D\,T^3+E\,T^4 \eqno(15)$$

$$\frac{\mu}{P_{2}c} = A + BT + CT^2 + DT^3 + ET^4$$
 (16)

In contrast to air, for steam the Peng-Robinson equation is used and solved numerically [49] to calculate the density as a function of temperature and pressure as the result is comparable to the International Water and Steam Tables of the International Association for the Properties of Water and Steam (IAPWS-IF97) [55]. The other thermophysical properties (c_p , μ , and λ) are interpolated using the tabulated values from the IAPWS-IF97. We used a cubic interpolation scheme for the temperature dependence and a linear interpolation for the pressure.

For the solid bauxite particle filler, a temperature dependence for the thermal conductivity and specific heat capacity is considered, and the material density is assumed to be constant over the investigated temperature range. A linear temperature correlation is used for the thermal conductivity based on published data [49] and a polynomial function [56] is used for the specific heat capacity which is in the range of published data for bauxite particles [57], see Equation (17) and (18).

$$\begin{split} c_{p,s} &= -2.853 \bullet 10^{-9} \, T^4 + 10.176 \bullet 10^{-6} \, T^3 - 12.8567 \\ &\bullet 10^{-3} \, T^2 + 7.41742 \, T + 581.327 \end{split} \tag{17}$$

$$\lambda_s = -9 \bullet 10^{-5} \, T + 2.1126 \tag{18}$$

2.5. Boundary and initial conditions

The equations are solved fully implicitly using the finite volume method in a linear algebraic equation solver in Python, using the same

boundary conditions as in our previous study [46]. However, an elevated temperature of 200–300 °C for the model validation and 600 °C for the parametric study are given as initial conditions for the solid temperature. Hence, a uniform temperature of $T_s=600\,^{\circ}C$ in the solid particle domain, see Equation (2), is considered as initial conditions. Losses through the insulation are considered by calculating the thermal transmittance coefficient U (Equation (8)) with the 600 °C as the interior temperature of the solid particles.

2.6. Mesh independence study

A spatial discretization element size of $\Delta z=2.5\,\text{mm}$ and a simulation time increment of $\Delta t=1\,\text{s}$ is used for the model validation. For the utility scale TES analysis, $\Delta z=5\,\text{mm}$ and $\Delta t=5\,\text{s}$ is used. A mesh independence study has been conducted by adjusting the mesh and time step size by a factor of 1/2. The independence study is showing reasonable accuracy for the selected spatial discretization sizes and time steps. The results show a median temperature difference between the simulation cases of less than 2 K which is within the accuracy range of the thermocouples installed in the experimental setup. A further reduction in spatial discretization element size would increase the computational time. Consequently, the mesh is considered sufficiently fine.

2.7. High-temperature electrolysis impact analysis

To determine the H_2 production rate \dot{n}_{H_2} of a high-temperature electrolysis, the electrical operating conditions are defined as a function of temperature. For low degradation, the cell voltage U_{cell} is equal to the thermoneutral voltage U_{tm} calculated with Equation (19) and (20) using the Faraday constant F. U_{cell} is calculated using the ideal cell voltage U_{ideal} (Equation (21) and the potential losses due to the cell area specific resistance ASR (Equation (22)) and the current density j (Equation (23)).

$$U_{cell} = U_{ideal} - jASR_{T_{cell}}$$
 (19)

$$U_{tn} = \frac{\Delta H}{2F} \tag{20}$$

The ideal cell voltage is calculated using the Nernst Equation (Equation (21)) and ASR. The ASR depends on the cell structure. For an electrode supported cell, Equation (22) is used with ASR $_0=0.2515\,\Omega\,\text{cm}^{-2},\,T_{ref}=1073.15\,\text{K},$ and $E_{ASR}=80674$ [58]. The current density is therefore calculated using Equation (23). The hydrogen production rate can then be obtained.

$$U_{ideal} = \frac{\Delta G}{2F} + \frac{RT_{cell}}{2F} ln \left(\frac{p_{H_2} \sqrt{p_{O_2}}}{p_{H_2O}} \right)$$
 (21)

$$ASR = ASR_0 exp\left(\frac{E_{ASR}}{R}\left(\frac{1}{T_{cell}} - \frac{1}{T_{ref}}\right)\right) \tag{22}$$

$$j = \frac{\dot{n}_{H_2}}{2F} \tag{23}$$

Using the TES outlet temperature during discharge as an input variable for cell temperature $T_{\rm cell}$, the hydrogen production rate can be calculated considering constant thermoneutral operation. In contrast,

 Table 1

 Polynomial coefficients for the thermophysical property calculation of air.

Parameter	A	В	С	D	E	F	G
c _p λ	2548.9320 -0.9080	3.5248 0.11161	-0.6366 -0.084333	-3.4281 0.056964	49.8238 -0.015631	-120.3466	98.8658
μ	-0.01702	0.79965	-0.72183	0.0496	-0.01388		

considering a constant TES outlet flow rate and a constant steam conversion rate of 70 %, the electrolysis shifts to an exothermal operation mode as the cell temperature is decreasing. The exothermal operation results in additional heating of the electrolysis streams causing a temperature increase from inlet to outlet. The amount of heating and the effective cell temperature results from an energy balance according to Equation (24) with the electrical cell power P_{cell} , the chemical energy demand of the water splitting reaction \dot{Q}_{chem} , and the in- and outlet thermal energy flow \dot{Q}_{in} and \dot{Q}_{out} , respectively. The calculation of the energy balance follows the methodology of Seitz et al. [15].

$$P_{cell} + \dot{Q}_{chem} + \dot{Q}_{in} + \dot{Q}_{out} = 0 \tag{24}$$

The impact of the temporal temperature gradient on the electrolysis operation is analyzed not only for the experimental investigation but also for an upscaled TES. The gradient is defined by the difference in discharge temperature between a defined time period during the discharge. For the upscaled TES investigation, the storage is charged with an inlet temperature of 850 °C and discharged with 600 °C for ten consecutive cycles to achieve stable temperature profile within the storage. While the experimental setup is designed for a steam temperature of 811 °C for steam and 863 °C for air [28], temperatures of 850 °C are achievable and are therefore used as a reference for the numerical analysis and investigation. The end of charging and discharging is defined by the storage outlet temperature: The storage outlet temperature must not exceed 600 °C during the charge phase and must not drop below 750 °C during the discharge phase to ensure a stable thermocline behavior [59]. Therefore, reaching these temperatures mark the end of charge or discharge of the storage. By ten consecutive charge and discharge cycles, the TES thermocline is considered to be stable [39,59]. Afterwards, flow rate adjusted operation can be investigated with a stable thermocline as the starting condition. Therefore, different TES aspect ratio AR = L/D equal to 1 and 4 are compared for a MW scale process. The storage volume is assumed to be the same for both AR. For the AR = 4, the storage height is 10 m. Thus, no measures to protect the insulation from thermo-mechanical stresses are required [60]. The volume of the TES is therefore 49.09 m^3 with a storage diameter of 2.5 m. The storage geometry for an AR of 1 result in a height and diameter of L = D = 3.9685 m. During charging, the nominal flow rate is 1.3399 kg/s for steam as the heat transfer medium. This mass flow results in a thermal power of 1 MW. When the TES is discharged with air, the flow rate is 2.3842 kg/s to obtain an equimolar flow rate at the inlet of the electrolysis. This ensures that the oxygen concentration at the outlet of the electrolysis is less than 40 % in the air stream.

3. Process description and experimental design

An experimental investigation is conducted for the evaluation of the process design and the interaction of different components. Fig. 1 shows the P&ID of the entire experimental setup. In the solar cavity receiver, water is evaporated and superheated. Simultaneously, an air stream is heated in the same device. Both, the steam and air are heated to temperatures above 800 °C. A steam accumulator is used to reduce pressure fluctuation from the evaporation process before the superheating of the steam. The cavity receiver design has been thoroughly investigated in a numerical analysis [29,61] and the experimental results as well as the analysis of the operational conditions of the receiver are beyond the scope of this study but are reported in [28]. Since the experiment is not physically coupled with a HTE, all process streams are released to the environment. When the solar thermal process is coupled with an electrolysis, the high temperature air and steam are used as inlet streams of the air and fuel electrode, respectively. In this work, the TES operation is analyzed. Therefore, the outlet flow conditions of the receiver are used as an input. Steam is used as a heat transfer fluid during the charging and air during the discharging phase of the TES.

3.1. Thermal energy storage design

The TES design is based on a numerical analysis to allow a charge and discharge duration of up to 3 h. Fig. 2 shows the general design of the packed bed storage device. The storage consists of three parts, the base with stands and a pipe, the central section including the thermocouple extensions for the temperature measurement, and the top with an additional pipe. The three sections are connected with flanges. A wired mesh is installed between the base and the central section. Thus, the particles bed is fixed inside the central section of the TES. Furthermore, there is no empty space at the top or bottom of the container, as it is completely filled with particles. With a maximum TES discharge flow rate of 40 kg/h, the calculated minimum fluidization velocity is always higher for the presented setup and according to Geldart [62], the combination of particle size and density difference makes it difficult to even fluidize the bed.

The experimental storage has a height of $L=0.632\,m$ and a diameter of D $\,=$ 0.263 m, and is filled with bauxite particles with a density of $\rho \,=$ 3560 kg/m³, average particle diameter of 0.578 mm, a particle shape factor of $C_{\rm f} = 1.09$, and an emissivity of $\epsilon = 0.9$ [57,63,64]. Meier et al. [65] suggests a diameter ratio $D/d_{p} > 40$ to limit the impact of the bypass in at the wall. Here, a diameter ratio of 455 is used and thus, a bypass of the particle bed at the near wall region due to the lower porosities can be neglected [49]. The bulk density of the bauxite particles was measured to be $2312.5 \,\mathrm{kg/m^3}$ resulting in a bed porosity of $\psi =$ 0.35. The key parameters of the storage and storage material are summarized in Table 2. To avoid condensation inside the storage, the tank was wrapped with electric heating cables and covered in 30 cm thick insulation made of Superwool® from Morgan Advanced Materials with a thermal conductivity at 600 $^{\circ}C$ of $\lambda_{ins}=0.13\,W/m/K$ [66]. The set temperature of the electric heating cables is 250 °C to avoid the condensation of steam during the charging phase of TES. The heat transfer to the particle bed is done be conduction only, as the heating cable are located at the exterior of the vessel beneath the insulation. The pre-heating has been done with enough time prior the experiment to ensure steady state conditions before initiating the charging. When exceeding the set temperature, the heating cable do not further heat the storage and the charging behavior of the TES is investigated.

The temperature distribution inside the storage is measured for the TES evaluation and model validation. Therefore, 12 N-type thermocouples are installed inside the particle bed. The pressure of each stream is measured with gauge pressure transmitters. Mass flows of air and water are controlled by mass flow controllers and the mass flow of steam is additionally measured by a mass flow meter. The uncertainty analysis is conducted based on the accuracy of each measuring and data acquisition device shown in Table 3. Assuming that the measurement error is normally distributed with random errors and a coverage factor of 1, the accuracy itself represents the measurement uncertainty [67].

The TES design is not optimized for the lowest pressure drop. Due to the diameter change from the piping from DN50 to the TES diameter of DN250 and the small particle size, an increased pressure drop is expected. For a reduced pressure drop, a diffuser section should be used to achieve an uniform flow profile across the TES diameter [68].

3.2. Experimental setup and testing conditions

The experimental setup in the Synlight® solar simulator at DLR is shown in Fig. 3. In Synlight®, 148 xenon short-arc lamps with an average radiation power of $2.5-2.7~\mathrm{kW_{rad}}$ [69,70] are used for the concentration of light on a target. The target of the present experimental setup is the aperture area of the solar cavity receiver. The lamps spectrum is close to the radiation spectrum of the sun, and peak flux densities of $12.5~\mathrm{MW/m^2}$ can be achieved [71]. 29 lamps corresponding to $72.5-78.3~\mathrm{kW_{rad}}$ are used in the actual experiment to heat up the inside of the solar cavity receiver and enable the device to generate high-

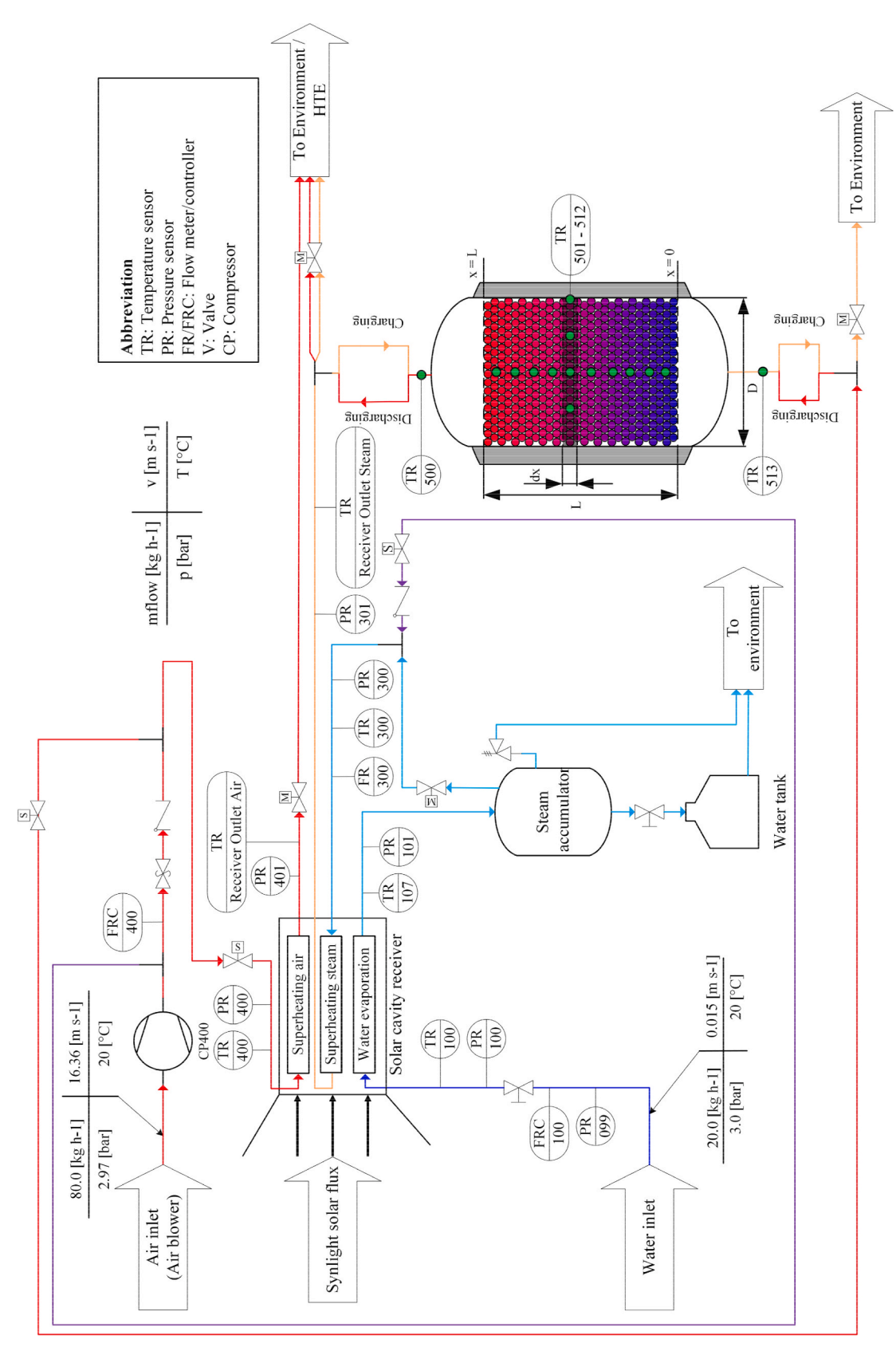


Fig. 1. P&ID of the experimental setup showing the solar receiver for the high-temperature steam and air generation and the high-temperature packed bed storage.

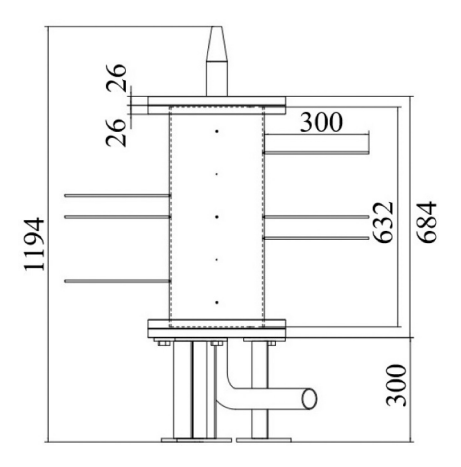


Fig. 2. Design of the TES assembly with dimensions in mm including the extensions for the thermocouple installation.

 Table 2

 Storage key parameters of the experimental setup and numerical simulation.

Parameter	Unit	Value
L	m	0.632
D	m	0.263
d_p	mm	0.578
d _{ins}	m	0.3
$\lambda_{ins}(600^{\circ}C)$	W/m K	0.13
$\rho_{Bauxite}$	kg/m ³	3560
C_{f}	_	1.09
ε	_	0.9
Ψ	_	0.35

Table 3 Experimental devices' accuracy and ranges. Where |T|, Rd, and FS indicate the actual temperature $[^{\circ}C]$, reading and full scale, respectively.

Experimental devices	Accuracy	Range
Pressure transmitter	±0.40 % FS	0-400 kPa (a)
Thermocouple (type N)	$\pm 0.004 T $	0–1100 °C
Mass flow controller (Water)	± 0.20 % Rd	0–30 kg/h
Mass flow meter (Steam)	$\pm 0.75 – 0.80 \text{ Rd}$	0–25 kg/h
Mass flow controller (Air)	$\pm 1.80~\%~FS$	0–85 kg/h
AD converter / Pressure transmitter module	± 0.76 % Rd	
AD converter / Thermocouple module	$\pm 2.33~^{\circ} C$	

temperature steam and air. Each lamp has a different focal point to make the heat flux distribution inside the cavity uniform. The whole experimental setup except for the receiver's aperture area is covered with the radiation shield (not shown in Fig. 3) to avoid any damages to the setup by the concentrated light. The thermal energy for the charging of the TES is provided by the receiver. The storage is charged from top to bottom with superheated steam generated inside the solar cavity receiver, while ambient air flows into the storage in the opposite direction from bottom to top during the discharge phase. The experiment was conducted in the following order:

1. Pre-heating of the TES to 200-300 °C

By this means, the heat transfer of sensible heat is investigated during the charging with steam as the condensation of the steam is avoided to the thermodynamic conditions.

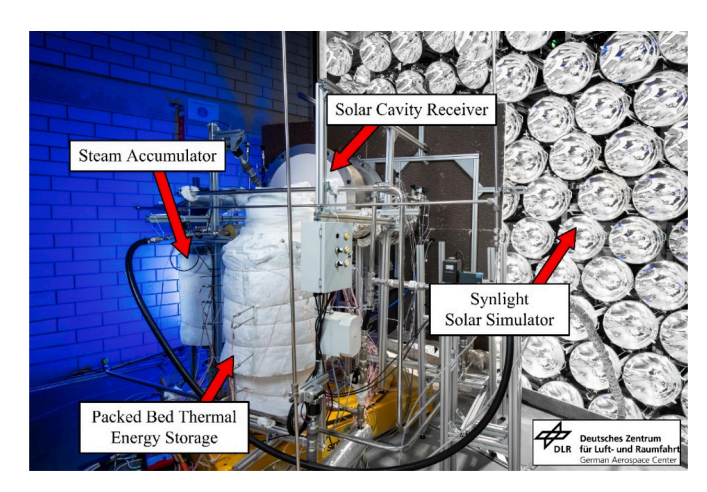


Fig. 3. Experimental setup of the solar thermal process in the Synlight® solar simulator.

2. Heating of the receiver with concentrated light

During the heating phase, the TES is not charged as the receiver outlet temperatures are low. Consequently, the streams to the TES are bypassed. The radiative power is increased incrementally until steady state outlet flow conditions at temperatures above 800 $^{\circ}$ C are reached.

3. Start of charging the TES

The start of charging is initiated. Therefore, the valves at the outlet of the TES are opened which allows for a flow through the TES. Then, the bypass line is closed and the entire steam mass flow is going to charge the TES.

4. End of charging the TES

As soon as the temperature at the bottom of the TES starts to increase rapidly, the TES charging ends before the exit temperature exceeds $600\,^{\circ}\text{C}$. Therefore, the bypass line is opened again and the TES outlet valve is closed again.

5. Receiver cooling

With an open bypass line, the receiver is cooled by turning off the lamps. Thus, no heat is provided to the receiver till the receiver reaches non-critical temperatures below 200 $^{\circ}\text{C}.$

6. Start of discharging the TES

When the receiver is cooled down, the air inlet to the bottom of the TES is opened, followed by closing the valves at the inlet of the receiver. As the bypass line is still open, the hot exit stream of the TES is released to the environment.

7. End of discharging the TES

The discharge is completed, when the TES exit at the top reaches a temperature below $200\,^{\circ}$ C. In conclusion, the TES is fully discharged and the experimental test campaign is completed.

While the TES can also be discharged with water or steam, it was neglected in the experimental setup to reduce process complexity. Furthermore, the TES would have to be bigger to be able to store the

thermal energy for the evaporation for the investigated flow rates. Additionally, the HTE requires both, steam and air. By switching the heat transfer media between charging and discharging all requirements can be met with such a design when two high temperature TES units are used.

4. Experimental results & model validation

Fig. 4 shows the temperature distribution in the axial direction of the TES over time for a complete charge and discharge cycle of the storage for one experimental test campaign. The red dotted curves are the measured temperatures in front of the flanges at TR500 and TR513, see Fig. 1. The red solid and dashed dotted lines are the first and last temperature sensors TR501 and TR512 inside the particle bed at the top and bottom, respectively. The temperature measurements of charging are shown for about 3 h, followed by the measurements of discharging phase. In between, a standby phase "receiver cooling" (see list in previous chapter) of the TES without any mass flow is measured and indicated by a grey area. Within this time period, the flow direction from top to bottom with steam for the charging is switched to the discharging with air in the opposite direction from bottom to top. During the experimental test campaign, steam and air temperatures of 811 °C and 863 °C were achieved at the receiver air and receiver steam outlets, respectively. However, the positioning of the receiver outlet is 2.5 m away from the TES and the thermal losses caused the temperature to drop to about 770 °C at TR500 before entering the packed bed TES. In addition, large flanges at the top and bottom of the TES are responsible for additional losses, reducing the final temperature entering the bed to below 750 °C. Furthermore, a non-uniform axial temperature distribution inside the storage is given as it can be identified by comparing the individual temperature at the beginning of the charging process in range of 15 to 60 min at 200–250 °C on the left-hand side in Fig. 4. A difference of up 50 K is measured as the external heating could not be controlled to achieve a uniform temperature distribution. Hence, a temperature wave is measured during the charging of the TES between 200–300 $^{\circ}\text{C}$ within the first 120 min of the measurement.

The dashed black lines, see TR505, TR506, and TR507, measure the radial temperature distribution at the axial center position. The radial offset temperature is slightly different from the black solid line in the center of the storage. This is because losses affect the radial temperature distribution due to the small storage size. However, as the difference is rather marginal, a good radial temperature and flow distribution can be considered.

The measured mass flow rates for the charge and discharge phases are shown in Fig. 5. The figure shows the raw measurement data, the one-minute moving average, and the lower and upper bounds of the sum of the moving average and the uncertainty of the measurement equipment. A peak in the steam mass flow is examined at the beginning of the charging phase. This is because the pressure in the tubes reduces when

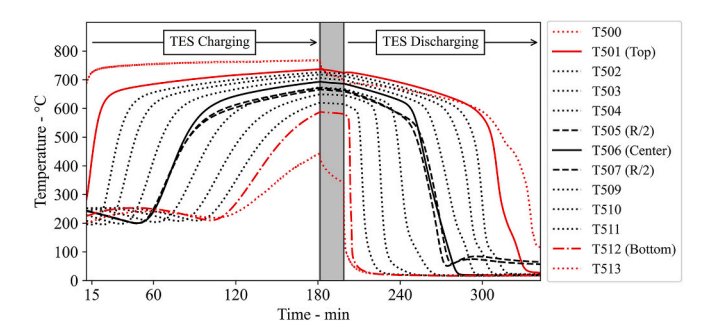


Fig. 4. TES temperature in axial position for a full charge and discharge cycle. The radial temperature change is shown as dashed lines for the center of the storage. The grey area in the center indicates the time needed to switch from the charging to the discharging phase.

the valve is opened to start charging. As a result, the low-temperature steam accumulator is drained, causing the mass flow to increase for a short time until the valve to the environment is closed. This effect does not apply to the air mass flow for the discharge phase of the system. During the charging phase, an average mass flow of 14.7 kg/h is used. The average charging power is $5.82\,\mathrm{kW}$ for an average discharge temperature of $750\,^\circ\mathrm{C}$, and due to the pre-heating of the TES, a low reference temperature of $200\,^\circ\mathrm{C}$. Thus, a storage capacity of $17.46\,\mathrm{kWh}$ is achieved with the presented TES design.

The discharging power is 7.64 kW for the same temperature at an average mass flow of 40 kg/h. Even though the mass flow during discharge is more than 2.5 times higher, the discharge power is only 1.3 times higher which is due to the average heat capacity: In the investigated temperature range, the heat capacity of steam is about 2 times higher than the one of air. Therefore, lower steam mass flow rates can be used to achieve the same thermal power. The relative pressure at the TES inlet during the experimental campaign is shown in Fig. 6 for the charge and discharge phase of the TES. The pressure is measured at the exit of the solar cavity receiver (PR301) during the charge and after the compressor (PR400) during the discharge. This measurement of pressure drop includes two valves, 2 m of piping (DN15), the inlet and outlet section of the TES with a change of diameter by a factor of 4, and the particle bed, leading to a relative pressure drop of 0.9 bar during charging and discharging. The pressure drop caused solely by the particle bed is calculated with the Ergun equation (Equation (7)), using the mean particle bed temperature and the flow rate of steam and air during the charge and discharge, respectively.

While the calculated particle bed pressure drop increases during the charging phase by 0.1291 bar over the full duration of charging, the measured pressure drop does not increase the first 120 min of charging but increases afterwards by 0.1781 bar.

In contrast, the measured and calculated pressure is decreasing during the discharging phase. The change in pressure at PR400 is -0.2988 bar, while we calculated a pressure drop due to the particle bed of -0.5372 bar.

At this point it should be noted that the TES design has not been optimized to minimize the pressure drop. Nevertheless, the pressure increase during the charge will have a neglectable effect on the opportunity cost as water is pumped in its liquid state before it is evaporated. For the compression of air by 1 bar, a specific energy demand of 59.7 kJ/kg is required for an isothermal compression. During an equimolar electrolysis operation, the energy of compression would be equivalent to 1.1 % of the energy content of the produced hydrogen.

4.1. Temperature gradient during the TES discharge

The outlet temporal temperature gradient during the discharge phase of the storage is studied as it is important for the safe operation of the high-temperature electrolysis. Fig. 7 shows the actual temperature profile measured at TR501 in Fig. 4 from minute 190 till the end of the measurements in the particle bed in red. Furthermore, the resulting temporal temperature gradient is shown in blue. After approximately 95 min of constant discharge power, the temperature gradient reaches the −5 K/min mark. During the discharge period, the average temperature gradient is $-1.3 \, \text{K/min}$. The temperature gradient is mainly caused by the charging phase of the storage, as the storage was charged at an increasing temperature over time. In addition, thermal losses and thermal diffusion increase the temperature gradient introduced by charging. Thus, a temperature gradient in the range of 0 to $-1\,\mathrm{K/min}$ is likely achievable with larger scale and better insulation properties. In addition, the discharge flow rate can be reduced, which will also help to improve the temperature gradient.

4.2. Model validation

For model validation, the 1-minute moving average mass flow rate

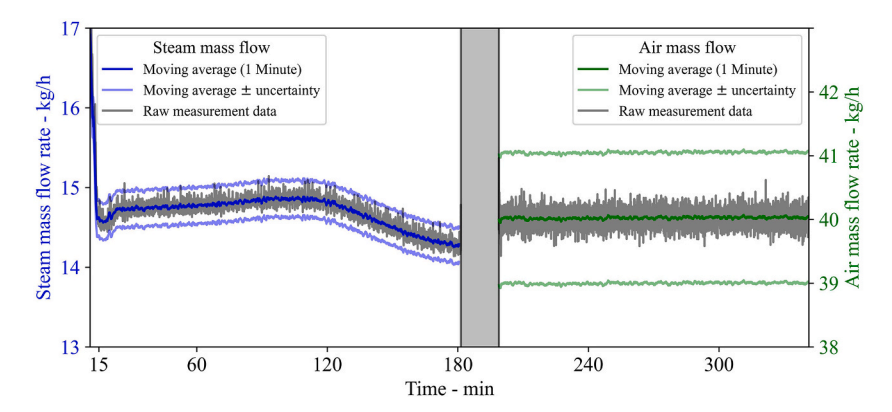


Fig. 5. Mass flow rates during charging with steam and discharging with air.

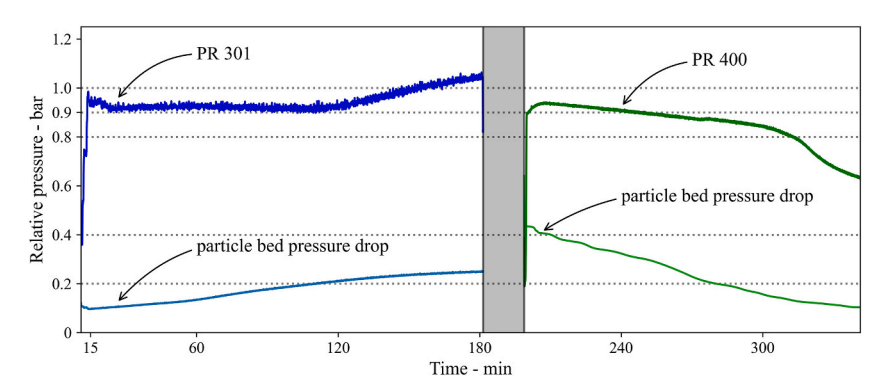
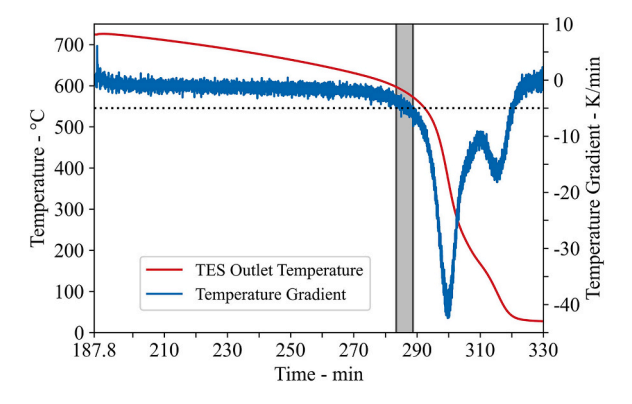


Fig. 6. Measured pressure at the inlet section of the TES during the charge and discharge phase and the calculated pressure drop of the particle bed using the Ergun equation.



 $\begin{tabular}{ll} Fig.~7. Experimentally measured TES outlet temperature (T501) during the discharge and the resulting temperature gradient. \\ \end{tabular}$

from Fig. 5 is used within the model. In addition, the inlet temperature is set to the measured temperature at the top of the packed bed instead of the actual inlet temperature, which was measured as well. This is due to the fact that the inlet temperature measured during the experimental test campaign is heavily influenced by the thermal mass of the flanges, which are not modelled in this study. Therefore, the temperature within the bed is more appropriate for modelling purposes. However, the first thermocouple is located approximately 7 cm below the surface of the particle bed and not at the top of the bed. To account for this distance, the average response time of the installed thermocouples is calculated, resulting in a time offset of approximately 12 min, as this is the time it takes for the next sensor to measure the same temperature. Increasing the mass flow rate would decrease this time delay by increasing the charging power for the same storage capacity. For the validation, the

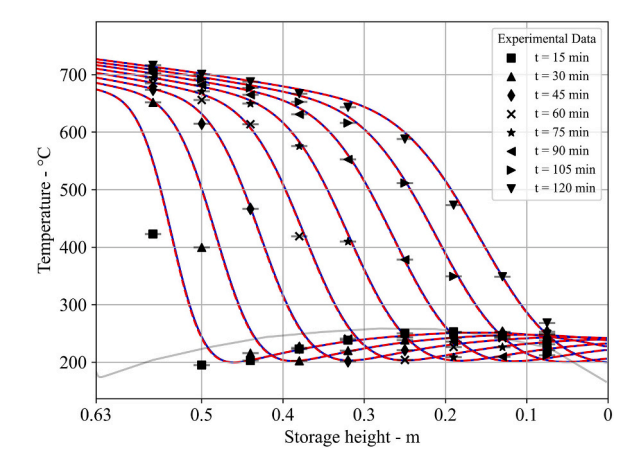


Fig. 8. Experimentally measured temperatures and numerically modeled temperature profiles along the axial axes of the thermal energy storage during the charging with steam as heat transfer media. Red color corresponds to the solid media and the blue color to the heat transfer media. The grey line shows the initial temperature distribution. (For interpretation of the references to colour in this figure legend, the reader is referred to the web version of this article.)

input temperature is set to the temperature measured at TR501, but the first 12 min are neglected and $T_{\rm inlet}(t_0) = T_{501}(t_0+12 \text{min}).$ Fig. 8 shows the modelled temperature profiles for the solid and liquid phases in red and blue, respectively. Additionally, black markers representing thermocouples from the experiment are plotted at the same times over the entire storage height. The markers also show an error bar corresponding to an uncertainty in thermocouple placement of $\pm 1\,\text{cm}$ due to possible

repositioning of the thermocouples during the filling process and thermal expansion of the bulk. Overall, the model can accurately predict the temperature profiles for most positions. A discrepancy between the calculated temperature profiles and the experimentally measured temperatures can be seen for the first two plots at 15 and 30 min compared to the other plots. The reason for this could be an overestimation of the inlet temperature at the beginning of the charging phase or an inhomogeneous heated particle bed. Nevertheless, the present model correlates with the experimentally measured temperatures for charging with steam. Furthermore, the wave motion of the initial temperature shows the same motion behavior for the experiment as well as for the numerical simulation.

For the discharge validation it is important to validate the TES outlet temperature behavior. The TES outlet temperature is directly impacting the electrolysis operation as the temperature determines the thermodynamics of the water splitting reaction. Fig. 9 shows the comparison of the measured temperatures at the top (T501) and bottom (T512) of the TES in black lines and the numerically calculated temperatures at the same position in red. Focusing on the temperature profile at T512, it can be seen that the numerically calculated temperature is slower than the experimental measured. In the experimental setup, the inlet of the TES has a diameter of 59 mm entering a particle bed with a diameter of 263 mm. Thus, a cold plug flow is entering the bed which can cause a cold channel in the center of the TES which cannot be investigated with the one dimensional model [72]. Nevertheless, the discharge temperature behavior of the TES at position T501 is calculated with an accuracy of 5.29 \pm 1.86 K. At the end of discharge, the difference is increasing significantly, which is caused by the thermal masse of the flanges used. The flanges are not considered in the model and therefore, the temperature is decreasing faster than in the experiment. Nevertheless, the model is suitable for the investigation of the TES discharge behavior as the calculated TES discharge temperature fits to the measured ones within the relevant operating behavior (see zoomed area), which is unaffected by external influences such as the heat capacity of the flanges or the introduced plug flow. To conclude, the model is validated with the experimental results and can be used to study modifications of the process parameters and the storage design, as long as the media specific thermophysical properties are used.

5. Electrolysis impact analysis

For the further analysis we assume that the TES can also be discharged with steam instead of air or, alternatively, a heat exchanger is used to utilize the discharge energy from the air stream to the steam stream. Of course, the system must be engineered accordingly which was not feasible for the presented experiment. Nevertheless, the experimental campaign in combination with the numerical analysis showed

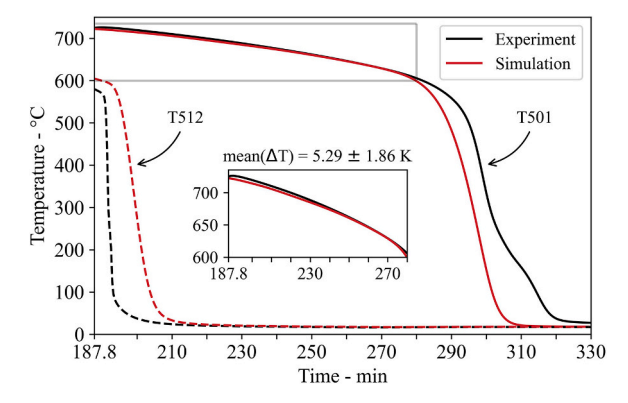


Fig. 9. TES discharge inlet and outlet temperature at T512 and T501 during the whole discharge period. Comparison between experimental measurements in black and simulation in red. (For interpretation of the references to colour in this figure legend, the reader is referred to the web version of this article.)

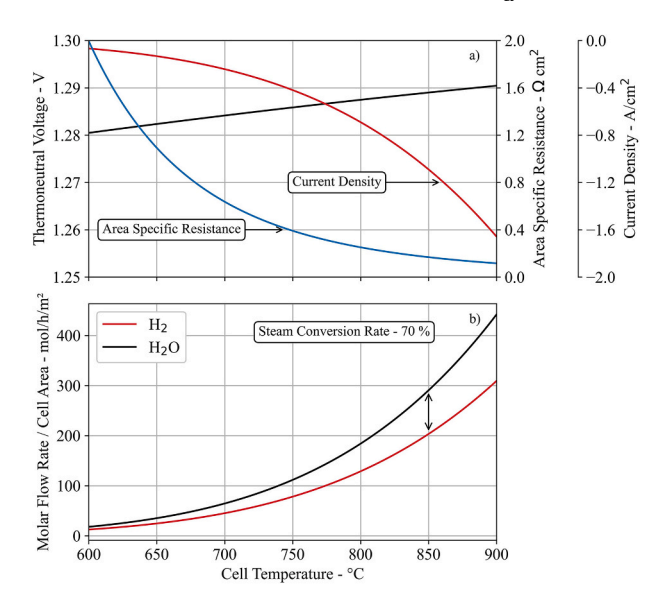


Fig. 10. Temperature dependent solid oxide cell operation behavior. a) Electrical operation conditions as function of temperature. b) Reactant and product cell area specific molar flow rate for a constant steam conversion rate.

similar TES operating conditions for steam and air.

In general, the hydrogen production rate increases with rising temperature as the area specific resistance decreases and therefore, more electrical energy is used for the actual water splitting reaction. Fig. 10 shows the temperature dependent electrical operating conditions of the solid oxide cell (a) and in (b) the resulting cell area specific molar flow rate for the reagent gas steam and the resulting product gas hydrogen for a constant steam conversion rate of 70 %. The area specific resistance is higher at lower temperatures. Therefore, ohmic losses will be higher, resulting in lower current densities to maintain thermoneutral operating conditions. Thus, the reagent gas flow rate is reduced to maintain constant conversion rates.

The electrolysis operating conditions depend on the temperature during the TES discharge, which decreases with time. The temperature decline increases the area specific resistance, resulting in a change in current density to maintain thermoneutral operating conditions from $-0.8~\text{A/cm}^2$ at 815~C to $-0.4~\text{A/cm}^2$ at 745~C. This change in current density results in a lower hydrogen production rate (Equation (23)). Fig. 11 shows the impact of temperature on the hydrogen production rate due to changes in temperature and hence current density of the TES system. The two solid horizontal lines show the constant molar flow rate for steam and air. The electrolysis inlet flow rate is equimolar as $\dot{n}_{\rm H2O+H2} = \dot{n}_{\rm Air}$. Also shown is the potential hydrogen production rate at nominal operating conditions with a steam conversion rate of 70 %.

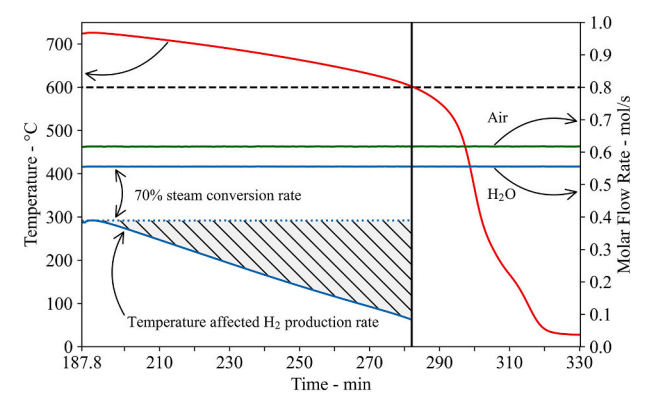


Fig. 11. Experimental storage discharge temperature (T501) impact on the electrolysis hydrogen production rate at continuous thermoneutral operation.

Compared to the nominal operation, the steam conversion rate can be reduced to less than 20 % of the starting production rate due to the temperature changes. For a temperature adjusted electrolysis operation, the amount of hydrogen produced drops from 5.17 kg (at constant steam flow rate, temperature, and steam conversion rate) to 2.85 kg, i.e. 55 %. Thus, the difference in production rate is indicated by the patterned area between the temperature adjusted and nominal hydrogen production rates. However, the declining temperature causes a shift towards an exothermal operation as the area specific resistance of the electrolysis cell is increasing, resulting in a higher electrical load.

The electrolysis operation analysis for the experimentally measured TES discharge behavior revealed a potential difference in $\rm H_2$ production rate between a constant and a temperature adjusted flow rate. In order to maintain high steam conversion rates and efficiently utilize the thermal energy of the storage system, the discharge flow rate should be adjusted according to the temperature changes. Changes in TES scale have been investigated and the impact of a large-scale TES discharge behavior is analyzed numerically with the validated model. Two different geometries with an AR of one and four are analyzed using air or steam as discharge heat transfer medium at equimolar flow rate. Fig. 12 shows the resulting temperature distribution inside the TES at different time points Δt . The figure is divided into four sub-figures for the different combinations of AR and heat transfer medium. The figure shows the

resulting temperature profile at constant flow rate as black dashed dotted lines. Additionally, the temperatures for the flow rate adjusted discharge are shown in red and blue for an AR of one and four respectively. The adjusted discharge flow rate is a result of the temperature and therefore the operating conditions of the electrolysis. Comparing the results of the different combinations, it can be seen that the thermocline is steeper at an AR of 4 than at an AR of 1. Furthermore, the discharge duration is longer when air is used as the heat transfer medium instead of steam. While the density of high-temperature steam and air have a similar temperature dependence, the specific heat capacity of steam increases faster than that of air with increasing temperature. Steam also has a higher specific heat capacity than air. As the electrolysis is operated equimolar, i.e. 1 mol of 90 % H_2O+10 % H_2 and 1 mol of air are required at the different electrolysis electrodes during its operation, different flow rates are used for the TES discharge. Therefore, a longer discharge time is achieved when air is used as the heat transfer medium and both TES are discharged at a flow rate sufficient to achieve an equimolar flow rate at the electrolysis inlet.

The results shown in Fig. 13 are based on the flow rate adjusted results presented in Fig. 12. As the discharge duration is different for the two media, a weighted mean temperature \overline{T} is calculated for the TES outlet temperature, shown in Fig. 13 a) for the different TES aspect ratios (AR = 1, AR = 4). The TES with a higher aspect ratio is affected more by

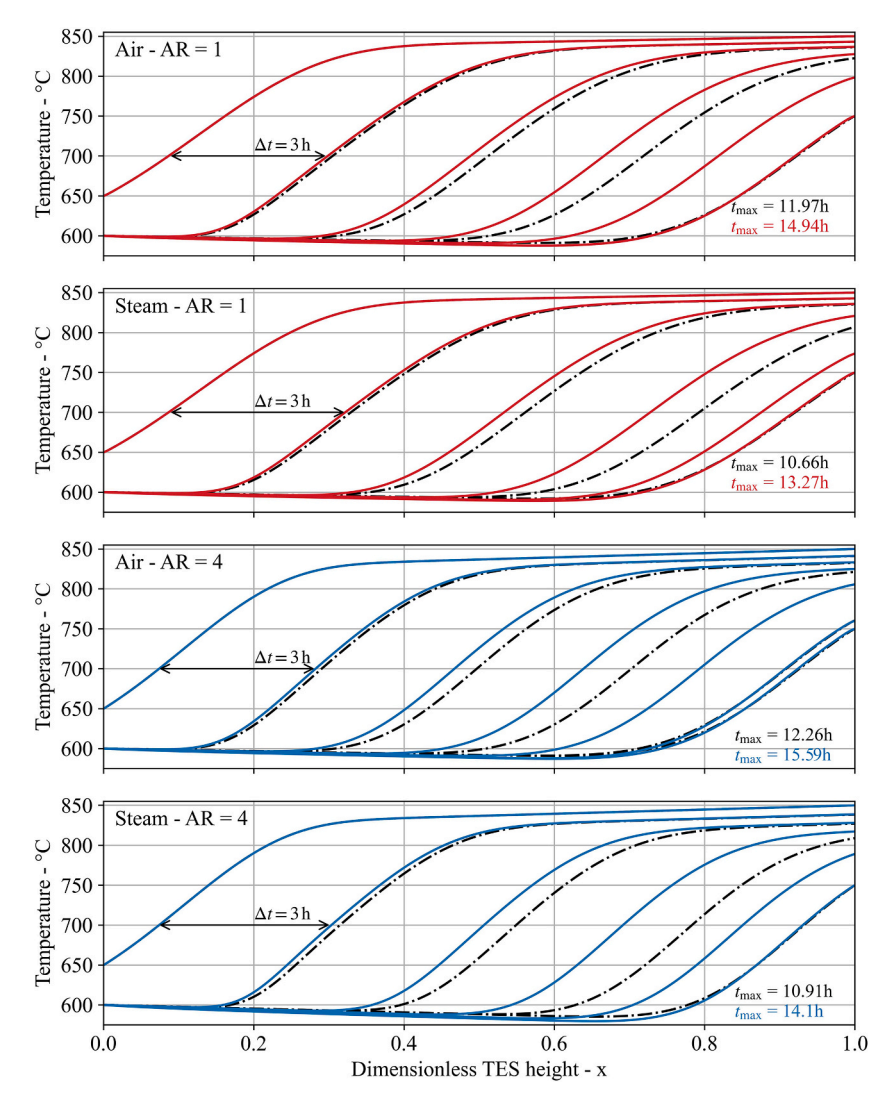


Fig. 12. TES discharge temperature profile at different aspect ratios (AR) using air and steam as discharge heat transfer media at an equimolar flow rate. The dash-dotted lines show the discharge behavior at constant flow rate and the colored solid lines the discharge behavior according to the electrolysis operation conditions adjusted flow rates. t_{max} denotes the maximum discharge duration of the storage under the given conditions.

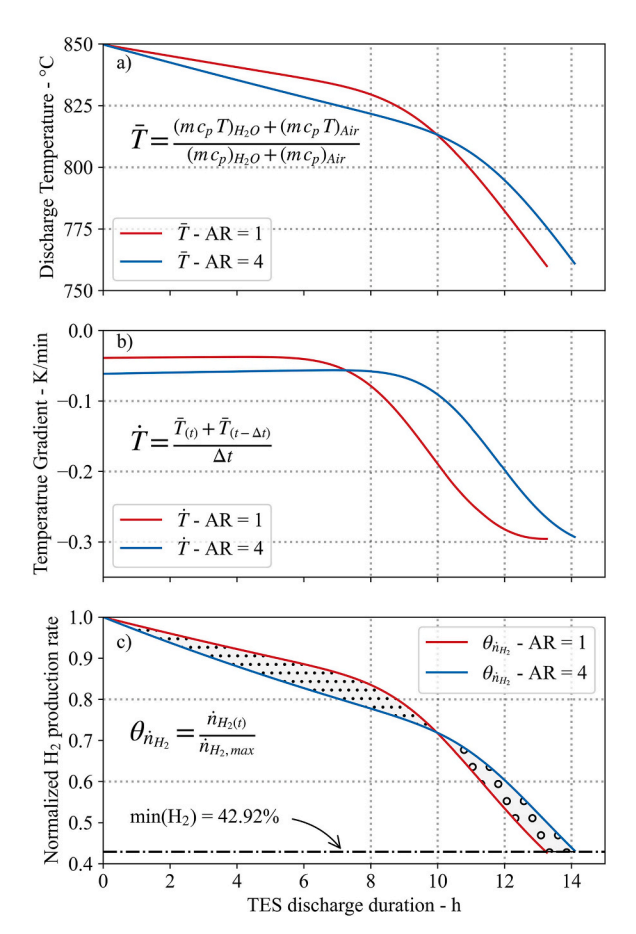


Fig. 13. Mean temperature (a), temporal temperature gradient (b), and normalized hydrogen production rate (c) during discharge of the TES with different aspect ratios (AR).

thermal losses because the volume specific surface area is higher than at lower ARs, which can also be seen from the temporal temperature gradient in Fig. 13 b). However, a longer discharge duration is achieved due to a better thermocline behavior with a higher aspect ratio [39]. Thus, the TES discharge behavior can be separated into two regimes. The first regime starts at t = 0 and defines a stable discharge temperature gradient which is caused by the thermal losses of the storage vessel. The second regime starts, when the temperature gradient changes as the outlet temperature decreases more intensively due to the thermocline movement inside the storage towards the outlet. The start of this effect is influenced by the steepness of the thermocline which is caused by the geometry. The higher the aspect ratio, the steeper the thermocline and therefore the longer the discharge duration at constant temperature gradient. Therefore, the difference in temperature behavior between the two geometries studied is an indicator of the difference in the resulting H₂ production rate using the weighted mean temperature, shown in Fig. 13 c). The patterned area indicate the production rate difference due to the difference in thermal losses and the change in thermocline behaviour. Both effects are caused by the difference in AR and therefore, the difference in geometry.

Improving the TES insulation will result in a reduction of the dotted patterned area, because the TES with a higher AR is affected more by thermal losses. In contrast, the circular patterned area is less affected as it is defined by the height of the TES, resulting from a better TES discharge performance for higher TES units. The axial heat transfer inside the particle bed is the same for both AR. However, a shorter storage height is experiencing a bigger relative effect in thermal dispersion than a higher storage height. Furthermore, the thermal dispersion is affected by the thermal losses. A sufficient insulation is essential to achieve

higher hydrogen production rates during the TES discharge. The tradeoff between the insulation investment cost and the change in hydrogen production rate needs to be optimized in future applications.

The highest pressure drop in the TES unit discharged by air occurs with an AR of 4. The pressure drop reaches it maximum at the beginning of the discharge phase with a similar behaviour as in Fig. 6, compare with Fig. 14. For an AR of 4, the pressure drop in the TES using air as heat transfer media is in its peak almost twice as high as when using steam with a relative pressure drop of 0.714 bar and 0.382 bar, respectively. The same can be identified for the AR of 1, with 0.099 bar when using air and 0.055 bar for steam. The difference in pressure due to the use of a different heat transfer media is caused by the difference in velocity. In the investigated temperature range, steam has a higher volumetric heat capacity than air which is almost twice as high. Thus, the velocity of air is higher than that of steam resulting in a higher pressure drop when flowing through the particle bed. Different measure can be taken, for example increasing the particle size or using lower AR to reduce the pressure drop. However, an economic optimization will determine the best TES design.

Fig. 15 shows the cumulative hydrogen production for the two geometries in comparison based on the TES outlet temperature as a reference to determine the electrolysis operating conditions. The solid lines show the production rate based on the weighted mean temperature for the same TES volume, one discharged with steam and another with air. Additionally, the dashed lines show the production rate based on the TES outlet temperature when discharged with steam (T_{H2O}). Furthermore, the theoretical production rate for a constant mass flow rate and constant current density (steam conversion rate) is shown as dashed dotted line with colored markers indicating the end of discharge for the different geometries, i.e. AR1 in red and AR4 in blue. Scaling both units to achieve the same discharge duration results in the same time dependency of the discharge temperature T_{H2O}. By adjusting the flow rate, the H₂ production rate is comparable to the theoretical production capacity. The difference in hydrogen production rate for the different aspect ratios is less than 1.7 %. Eventually, due to a higher discharge duration, AR = 4 is able to produce more. The difference in slope is caused by the thermal losses and can be optimized. The difference in H₂ production rate between the colored lines is due to the use of different temperatures. The weighted mean temperature \overline{T} is higher than the discharge temperature of the TES discharged with steam. The reason is the longer discharge duration of the air TES. While the storage geometry is the same, the discharge rate is differently maintaining the same molar flowrate for the electrolysis. Thus, the discharge power for the steam TES unit is higher than of the air TES. However, the air and steam TES can be scaled relative to each other so that they have the same maximum discharge duration. The resulting H2 production capacity is lower than in the case with constant flow and steam conversion rate as it can be seen in Fig. 15 by comparing the dashed lines with the colored markers on the

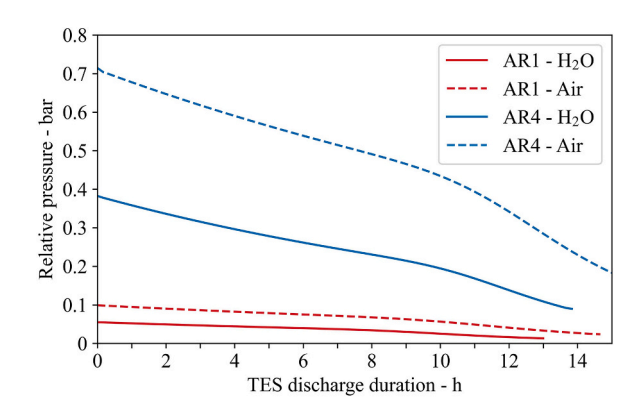


Fig. 14. Relative pressure drop for the different TES geometries with different heat transfer media during the discharge phase.

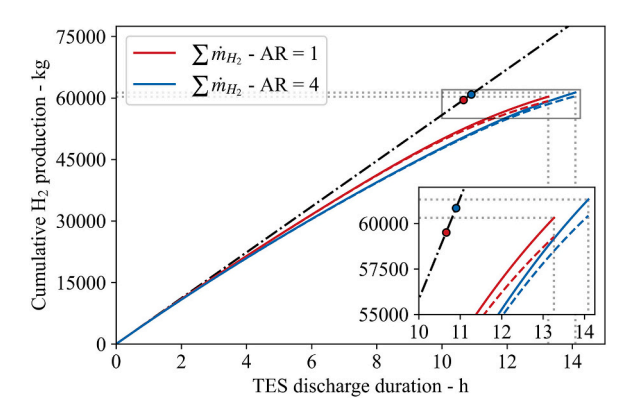


Fig. 15. Cumulative hydrogen production during the TES discharge for different aspect ratios (AR). The solid line is the production capacity based on the weighted mean temperature \overline{T} and the dashed line for using steam as reference temperature only. The colored markers on the dash-dotted line present the hydrogen production rate at constant flow rate and current density.

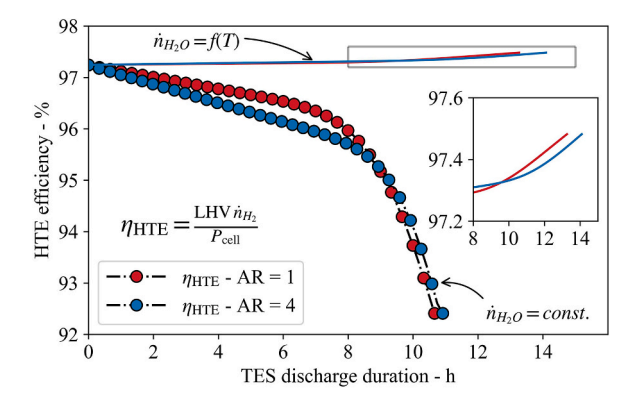


Fig. 16. HTE stack efficiency during TES discharge at constant and temperature adjusted steam inlet flow rates for a constant steam conversion.

dashed dotted line. This can be explained by the increase in thermal losses, because the TES system is discharged over a longer period.

The different operating conditions affect not only the hydrogen yield and operating time, but also the electrical energy demand. Fig. 16 shows the electrolysis stack efficiency as a function of the TES discharge duration and therefore as a function of TES discharge temperature. The dashed dotted lines with colored markers show the stack efficiency at constant inlet flow rate and constant steam conversion rate for the different TES discharge behaviors affected by the aspect ratio. The solid colored lines correspond to the HTE stack efficiency for a temperature

adjusted flow rate $\left(\dot{n}_{H_2O} = f(\overline{T})\right)$ to maintain thermoneutral electrol-

ysis operation at a constant steam conversion rate. When the electrolysis is operated at a constant flow rate and steam conversion rate, the electrical energy demand increases with the decline in temperature due to the increase in area specific resistance. When the flow rate is adjusted according to the decrease in temperature to maintain thermoneutral conditions, the electrical efficiency is almost constant when thermal losses are neglected. Therefore, temperature adjusted operation not only extends the operating time, but it also limits the electrical load. Similar to Sanz-Bermejo et al. [9], highest electrical conversion efficiencies are maintained in a load flexible HTE operation.

A constant flow and steam conversion rate would result in an exothermal electrolysis operation and thus reduced stack efficiency. The calculated current density is constant at $-1.09 \,\mathrm{A/cm^2}$ as the flow rate and steam conversion rate is constant. This cell has not been tested at current densities exceeding -0.8 A/cm^2 [58], but the cell voltage is within the operating range of exothermally operated cells [4] and future improvements are expected to achieve current densities in the range of -1 to -1.4 A/cm² and higher [5]. While the current density is constant, the voltage increases from 1.29 V to 1.38 V while the TES is discharging. The TES discharge temperature declines during the discharge which results in a higher cell resistance and therefore an increase in total cell voltage. The same behavior has been shown by Hwang et al. [25] showing an increase in current density affected by the TES temperature and an operation at constant current density. The change in current density is caused by the temperature dependency of the area specific resistance. Due to the increased area specific resistance with decreasing temperature and comparable high current density, the exothermal operation of the electrolysis is expected to increase the degradation rate. Therefore, external electrical heating is used to still enable thermoneutral operation. However, if the flow rate is not adjusted according to the TES discharge temperature, the total electrical energy demand will increase. From an economic perspective, the flow rate should be adjusted according to the discharge temperature to maintain thermoneutral operation for lower stack degradation and to limit the electrical energy demand by avoiding the use of additional electric heating. If we adjust the flow rate, we can maintain the thermoneutral operation conditions at almost constant cell voltage of 1.29 V. The current density ranges from -0.42 to -1.09 A/cm² in dependence of the flow rate and area specific resistance to achieve the thermoneutral voltage. Thus, the cell is less stressed by the current density and should degrade more slowly than an exothermally operated cell.

6. Conclusion

For a continuous thermoneutral or endothermal high-temperature electrolysis operation powered by fluctuating renewable energy sources, a high-temperature energy storage is required. In this paper, the use of solar-generated high-temperature steam and its interaction with a packed bed thermal energy storage system has been studied experimentally and numerically. Furthermore, an analysis of the effects on the electrolysis of steam and air discharged from TES was conducted on the basis of the validation results. The following points summarize the main results of the experimental and numerical analysis:

- \bullet A solar receiver (70 $kW_{th})$ and a thermal energy storage (17.46 $kWh_{th})$ were designed, built, and tested.
- The experimentally investigated temporal temperature gradient at the storage outlet was above –5 K/min for the first 100 min of the experimental discharge period. This is deemed sufficient for solid oxide cell electrolysis operation. Moreover, stable mass flow conditions were found during steam charging and air discharging.
- The developed numerical model is validated with the experimental results. The model shows that the temporal temperature gradient improved with increased scale of the TES to a maximum of -0.3 K/ min for a larger storage. The parametric study shows that the storage height should be maximized to prolongate the storage discharge duration and thus, the hydrogen production capacity during discharge.
- A temperature adjusted flow rate for constant thermoneutral electrolysis operation at a constant steam conversion rate results in a high hydrogen production capacity with electrical stack efficiencies above 97 %.

An experimental investigation of the TES discharge conditions that affect the electrolysis operation and thus the stack degradation is to be studied. Furthermore, the economic and environmental impact of the storage size for an optimized component scaling and $\rm H_2$ production will be investigated. Future work will also analyze the synergies of redox reactive storage material and the high-temperature electrolysis operation.

Data Availability Statement

Datasets generated in the study are available from the corresponding author on reasonable request.

CRediT authorship contribution statement

Timo Roeder: Writing – review & editing, Writing – original draft, Visualization, Validation, Software, Methodology, Investigation, Formal analysis, Data curation, Conceptualization. **Yasuki Kadohiro:** Writing – review & editing, Investigation, Formal analysis, Data curation. **Kai Risthaus:** Writing – review & editing, Supervision, Project administration, Methodology, Formal analysis, Data curation. **Anika Weber:** Writing – review & editing, Validation, Investigation, Data curation. **Enric Prats-Salvado:** Writing – review & editing, Resources, Formal

analysis. **Nathalie Monnerie:** Writing – review & editing, Supervision, Resources, Project administration, Investigation, Funding acquisition, Conceptualization. **Christian Sattler:** Writing – review & editing, Supervision, Resources, Funding acquisition, Conceptualization.

Declaration of Competing Interest

The authors declare that they have no known competing financial interests or personal relationships that could have appeared to influence the work reported in this paper.

Acknowledgment

The authors thank Fabio Pierno, Kai-Peter Eßer, Sebastian Melzer, Ewald-Ingo Radke and Dmitrij Laaber from Institute of Future Fuels, DLR for their support in the preparation of the experimental setup. This work was supported by the Ministry of Economic Affairs, Industry, Climate Action and Energy of the state of North Rhine-Westphalia and the Federal Ministry for Economic Affairs and Climate Action of the Federal Republic of Germany through their programs for structural transformation of the Rhenish mining area. The authors gratefully acknowledge the funding by the DLR internal project Solar Heat Supp. SOFC

Appendix

Experimentally measured data of four consecutive days including the important TES temperature for the electrolysis operation, the charge and discharge mass flow rates, and the relative TES charge and discharge pressures.

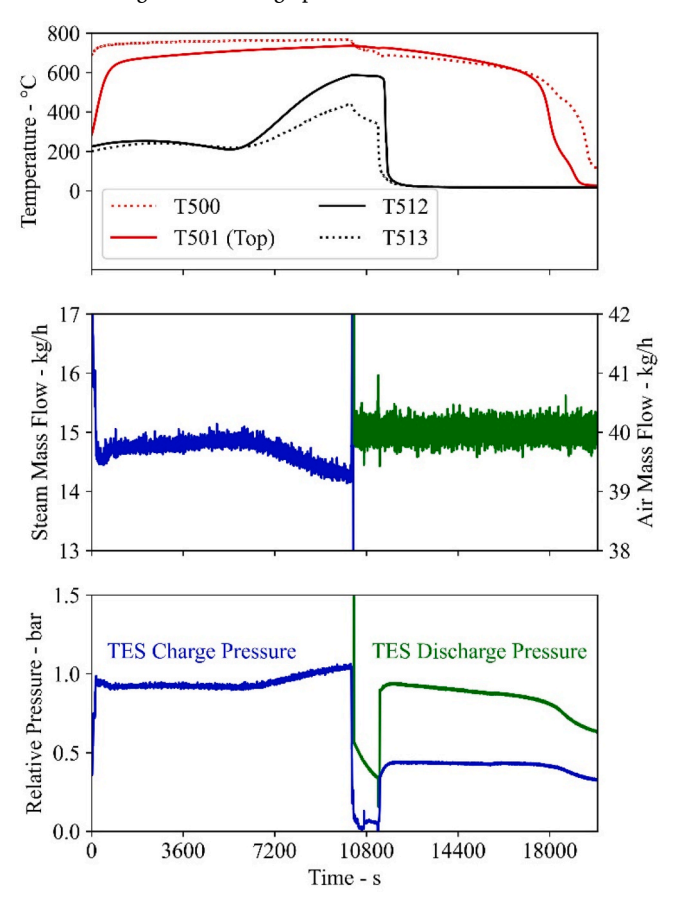


Fig. 18. Experimental data of the 1st day.

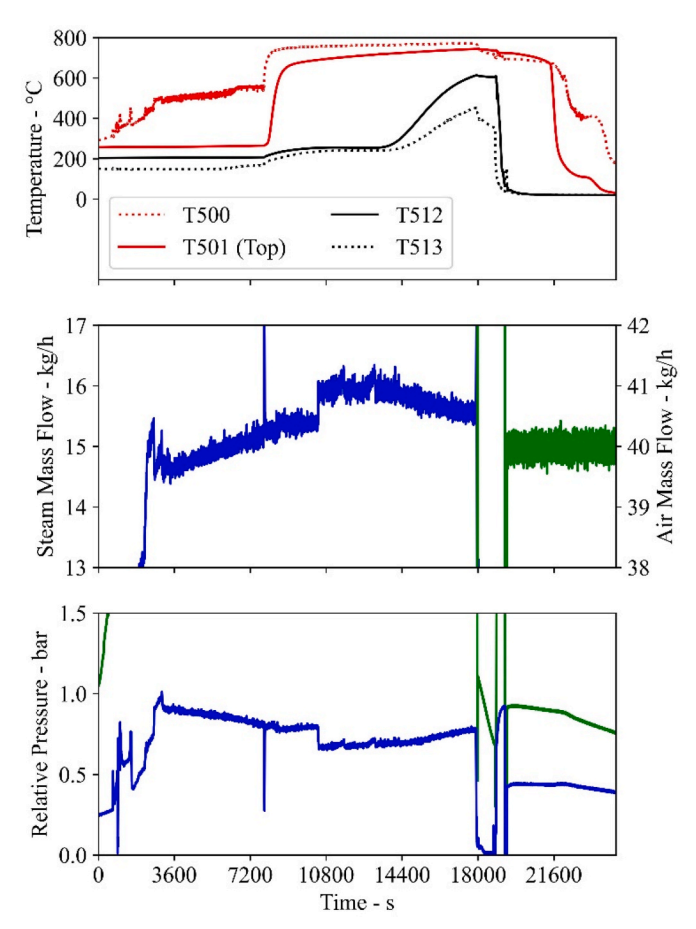


Fig. 19. Experimental data of the 2nd day.

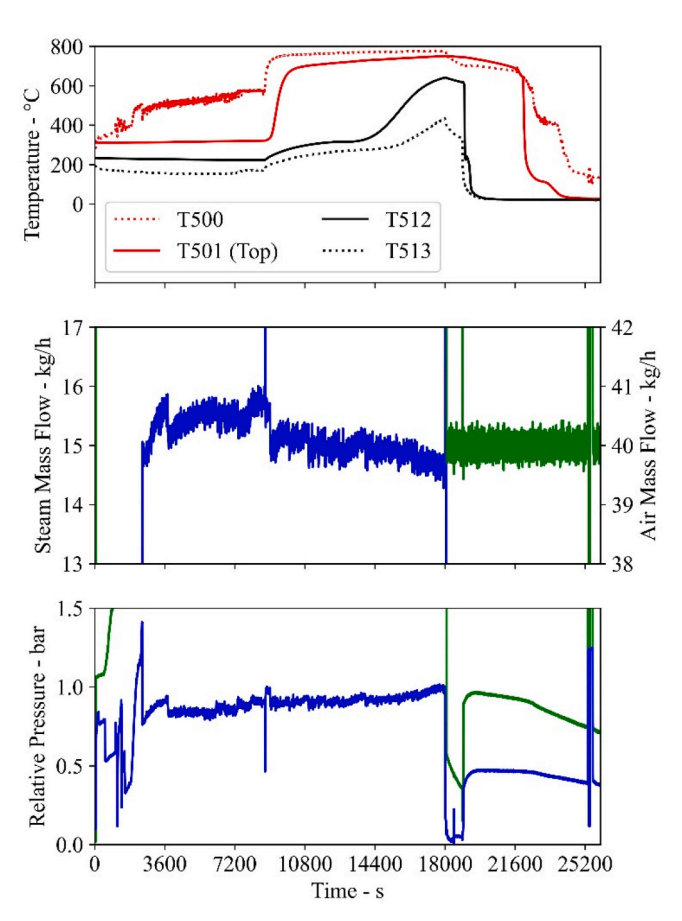


Fig. 20. Experimental data of the 3rd day.

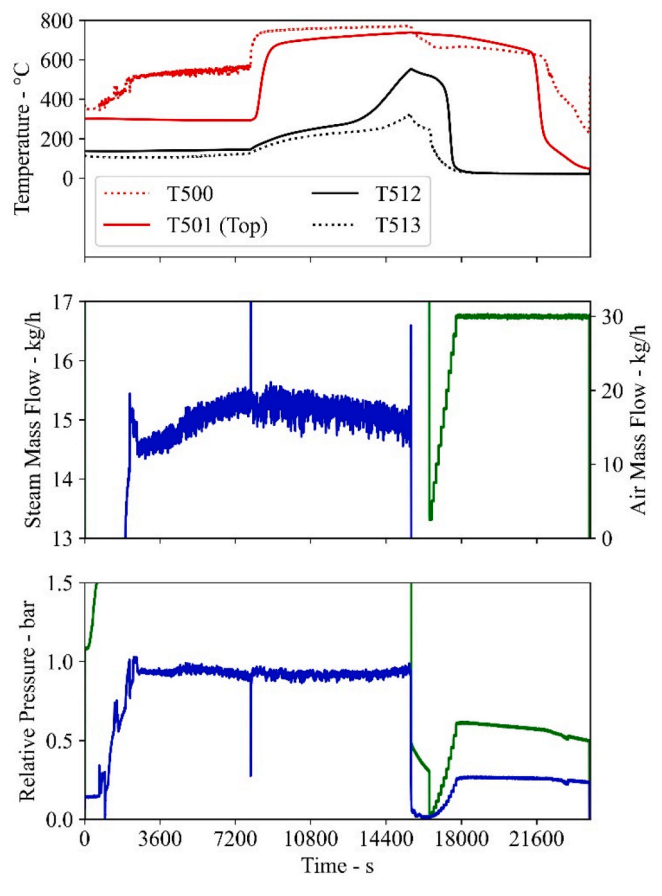


Fig. 21. Experimental data of the 4th day.

References

- Hydrogen Europe, Clean Hydrogen Monitor, 2023. Accessed: Aug. 11, 2025.
 [Online]. Available: https://hydrogeneurope.eu/wp-content/uploads/2024/11/ Clean_Hydrogen_Monitor_11-2023_DIGITAL.pdf.
- [2] IRENA, World Energy Transitions Outlook 2022: 1.5°C Pathway. International Renewable Energy Agency, 2022. 978-92-9260-429-5. Accessed: Mar. 5, 2025. [Online]. Available: https://www.irena.org/publications/2022/Mar/World-Energy-Transitions-Outlook-2022.
- [3] F. Petipas, A. Brisse, C. Bouallou, Benefits of external heat sources for high temperature electrolyser systems, Int. J. Hydrogen Energy 39 (11) (2014) 5505–5513, https://doi.org/10.1016/j.ijhydene.2014.01.179.
- [4] F. Petipas, A. Brisse, C. Bouallou, Model-based behaviour of a high temperature electrolyser system operated at various loads, J. Power Sources 239 (2013) 584–595, https://doi.org/10.1016/j.jpowsour.2013.03.027.
- [5] S.E. Wolf, et al., Solid oxide electrolysis cells current material development and industrial application, J. Mater. Chem. A 11 (34) (2023) 17977–18028, https:// doi.org/10.1039/D3TA02161K.
- [6] M. Lang, S. Raab, M.S. Lemcke, C. Bohn, M. Pysik, Long-Term Behavior of a Solid Oxide Electrolyzer (SOEC) Stack, Fuel Cells 20 (6) (2020) 690–700, https://doi. pxg.(10.1003/fsrs.201003/45.
- [7] T. Roeder, A. Rosenstiel, N. Monnerie, C. Sattler, Impact of expected cost reduction and lifetime extension of electrolysis stacks on hydrogen production costs, Int. J. Hydrogen Energy (2024), https://doi.org/10.1016/j.ijhydene.2024.08.015.
- [8] J. Sanz-Bermejo, J. Muñoz-Antón, J. Gonzalez-Aguilar, M. Romero, Optimal integration of a solid-oxide electrolyser cell into a direct steam generation solar tower plant for zero-emission hydrogen production, Appl. Energy 131 (2014) 238–247, https://doi.org/10.1016/j.apenergy.2014.06.028.
- [9] J. Sanz-Bermejo, J. Muñoz-Antón, J. Gonzalez-Aguilar, M. Romero, Part load operation of a solid oxide electrolysis system for integration with renewable energy sources, Int. J. Hydrogen Energy 40 (26) (2015) 8291–8303, https://doi.org/ 10.1016/i.jihydene.2015.04.059.
- [10] G. Puig-Samper, E. Bargiacchi, D. Iribarren, J. Dufour, Assessing the prospective environmental performance of hydrogen from high-temperature electrolysis coupled with concentrated solar power, Renew. Energy (2022), https://doi.org/ 10.1016/j.renene.2022.07.066.

- [11] N. Monnerie, H. von Storch, A. Houaijia, M. Roeb, C. Sattler, Hydrogen production by coupling pressurized high temperature electrolyser with solar tower technology, Int. J. Hydrogen Energy 42 (19) (2017) 13498–13509.
- [12] M. Roeb, N. Monnerie, A. Houaijia, C. Sattler, J. Sanz-Bermejo, M. Romero, I. Canadas, Anabella Drisaldi Castro, Cristina Lucero, Rocio Palomino, Floriane Petipas and Annabelle Brisse, "Coupling Heat and Electricity sources to Intermediate Temperature Steam Electrolysis,", Journal of Energy and Power Engineering 7 (2013) 2068–2077.
- [13] Z. Ma, J. Martinek, Integration of Concentrating Solar Power with High Temperature Electrolysis for Hydrogen Production, SolarPACES Conf Proc 2 (2024), https://doi.org/10.52825/solarpaces.v2i.973.
- [14] J. Immonen, K.M. Powell, Hydrogen from solar? a rigorous analysis of solar energy integration concepts for a high temperature steam electrolysis plant, Energ. Conver. Manage. 298 (2023) 117759, https://doi.org/10.1016/j. enconman.2023.117759.
- [15] M. Seitz, H. von Storch, A. Nechache, D. Bauer, Techno economic design of a solid oxide electrolysis system with solar thermal steam supply and thermal energy storage for the generation of renewable hydrogen, Int. J. Hydrogen Energy 42 (42) (2017) 26192–26202, https://doi.org/10.1016/j.ijhydene.2017.08.192.
- [16] J. C. Restrepo, D. Luis Izidoro, A. Milena Lozano Násner, O. José Venturini, and E. Eduardo Silva Lora, "Techno-economical evaluation of renewable hydrogen production through concentrated solar energy," *Energy Conversion and Management*, vol. 258, p. 115372, 2022, doi: 10.1016/j.enconman.2022.115372.
- [17] A.R. Razmi, A.R. Hanifi, M. Shahbakhti, Design, thermodynamic, and economic analyses of a green hydrogen storage concept based on solid oxide electrolyzer/fuel cells and heliostat solar field, Renew. Energy 215 (2023) 118996, https://doi.org/ 10.1016/j.renene.2023.118996.
- [18] G. Schiller, et al., Solar heat integrated solid oxide steam electrolysis for highly efficient hydrogen production, J. Power Sources 416 (2019) 72–78, https://doi. org/10.1016/j.jpowsour.2019.01.059.
- [19] W.-D. Steinmann and C. Prieto, "Thermal storage for concentrating solar power plants," in Advances in Thermal Energy Storage Systems, Elsevier, 2021, pp. 673–697.
- [20] W.-D. Steinmann, Thermal Energy Storage for Medium and High Temperatures, Springer Fachmedien Wiesbaden, Wiesbaden, 2022.
- [21] P. Mottaghizadeh, S. Santhanam, M.P. Heddrich, K.A. Friedrich, F. Rinaldi, Process modeling of a reversible solid oxide cell (r-SOC) energy storage system utilizing commercially available SOC reactor, Energ. Conver. Manage. 142 (2017) 477–493, https://doi.org/10.1016/j.encomman.2017.03.010.

- [22] M. Promsen, K. Selvam, Y. Komatsu, A. Sciazko, S. Kaneko, N. Shikazono, Metallic PCM-integrated solid oxide fuel cell stack for operating range extension, Energ. Conver. Manage. 255 (2022) 115309, https://doi.org/10.1016/j. encomman 2022 115309
- [23] A. Sun, et al., Self-adaptive heat management of solid oxide electrolyzer cell under fluctuating power supply, Energ. Conver. Manage. 271 (2022) 116310, https://doi. org/10.1016/j.enconman.2022.116310.
- [24] J. Hosseinpour, O.B. Rizvandi, R.J. Braun, Enhancing thermal management in a reversible solid oxide cell system utilizing thermal energy storage, J. Storage Mater. 114 (2025) 115806, https://doi.org/10.1016/j.est.2025.115806.
- [25] H. Hwang, Y. Lim, W. Choi, Reversible solid oxide cell system with thermocline-type thermal energy storage: Numerical and techno-economic analysis, Energ. Conver. Manage. 314 (2024) 118652, https://doi.org/10.1016/j.enconman.2024.118652.
- [26] L. Geissbühler, A. Mathur, A. Mularczyk, A. Haselbacher, An assessment of thermocline-control methods for packed-bed thermal-energy storage in CSP plants, Part 2: Assessment strategy and results, Sol. Energy 178 (2019) 351–364, https:// doi.org/10.1016/j.solener.2018.12.016.
- [27] L. Geissbühler, A. Mathur, A. Mularczyk, A. Haselbacher, An assessment of thermocline-control methods for packed-bed thermal-energy storage in CSP plants, Part 1: Method descriptions, Sol. Energy 178 (2019) 341–350, https://doi.org/ 10.1016/j.solener.2018.12.015.
- [28] Y. Kadohiro, T. Roeder, K. Risthaus, D. Laaber, N. Monnerie, C. Sattler, Experimental demonstration and validation of tubular solar cavity receivers for simultaneous generation of superheated steam and hot air, Appl. Energy 380 (2025) 125042, https://doi.org/10.1016/j.apenergy.2024.125042.
- [29] Y. Kadohiro, K. Risthaus, N. Monnerie, C. Sattler, Numerical investigation and comparison of tubular solar cavity receivers for simultaneous generation of superheated steam and hot air, Appl. Therm. Eng. 238 (2024) 122222, https://doi. org/10.1016/j.applthermaleng.2023.122222.
- [30] M. Lin, C. Suter, S. Diethelm, J. van Herle, S. Haussener, Integrated solar-driven high-temperature electrolysis operating with concentrated irradiation, Joule 6 (9) (2022) 2102–2121, https://doi.org/10.1016/j.joule.2022.07.013.
- [31] J. Edwards, H. Bindra, An experimental study on storing thermal energy in packed beds with saturated steam as heat transfer fluid, Sol. Energy 157 (2017) 456–461, https://doi.org/10.1016/j.solener.2017.08.065.
- [32] C. Suresh, R.P. Saini, Review on solar thermal energy storage technologies and their geometrical configurations, Int. J. Energy Res. 44 (6) (2020) 4163–4195, https://doi.org/10.1002/er.5143.
- [33] I. Calderón-Vásquez, et al., Review on modeling approaches for packed-bed thermal storage systems, Renew. Sustain. Energy Rev. 143 (2021) 110902, https://doi.org/10.1016/j.rser.2021.110902.
- [34] R. Cai, J. Dou, E. Krzystowczyk, A. Richard, F. Li, Chemical looping air separation with Sr0.8Ca0.2Fe0.9Co0.1O3-8 perovskite sorbent: Packed bed modeling, verification, and optimization, Chem. Eng. J. 429 (2022) 132370, https://doi.org/ 10.1016/j.cej.2021.132370.
- [35] R. Cai, E. Krzystowczyk, B. Braunberger, F. Li, L. Neal, Techno-economic analysis of chemical looping air separation using a perovskite oxide sorbent, Int. J. Greenhouse Gas Control 132 (2024) 104070, https://doi.org/10.1016/j. ijggc.2024.104070.
- [36] M. Pein et al., "Reticulated Porous Perovskite Structures for Thermochemical Solar Energy Storage," Advanced Energy Materials, vol. 12, no. 10, 2022, Art. no. 2102882, doi: 10.1002/aenm.202102882.
- [37] Q. Fu, C. Mabilat, M. Zahid, A. Brisse, L. Gautier, Syngas production via high-temperature steam/CO2 co-electrolysis: an economic assessment, Energy Environ. Sci. 3 (10) (2010) 1382, https://doi.org/10.1039/c0ee00092b.
- [38] C. Xu, Z. Wang, Y. He, X. Li, F. Bai, Parametric study and standby behavior of a packed-bed molten salt thermocline thermal storage system, Renew. Energy 48 (2012) 1–9, https://doi.org/10.1016/j.renene.2012.04.017.
- [39] M. Cascetta, F. Serra, S. Arena, E. Casti, G. Cau, P. Puddu, Experimental and numerical research activity on a packed bed TES system, Energies 9 (9) (2016) 758, https://doi.org/10.3390/en9090758.
- [40] C. Xu, X. Li, Z. Wang, Y. He, F. Bai, Effects of solid particle properties on the thermal performance of a packed-bed molten-salt thermocline thermal storage system, Appl. Therm. Eng. 57 (1–2) (2013) 69–80, https://doi.org/10.1016/j. applthermaleng.2013.03.052.
- [41] M. Hänchen, S. Brückner, A. Steinfeld, High-temperature thermal storage using a packed bed of rocks – heat transfer analysis and experimental validation, Appl. Therm. Eng. 31 (10) (2011) 1798–1806, https://doi.org/10.1016/j. applthermaleng.2010.10.034.
- [42] S. Tescari, et al., Numerical model to design a thermochemical storage system for solar power plant, Energy Procedia 75 (2015) 2137–2143, https://doi.org/ 10.1016/j.egypro.2015.07.347.
- [43] S. Tescari et al., "Experimental proof of concept of a pilot-scale thermochemical storage unit," p. 90006, 2017, doi: 10.1063/1.4984455.
- [44] P.A. Galione, C.D. Pérez-Segarra, I. Rodríguez, A. Oliva, J. Rigola, Multi-layered solid-PCM thermocline thermal storage concept for CSP plants. Numerical analysis and perspectives, Appl. Energy 142 (2015) 337–351, https://doi.org/10.1016/j. apenergy.2014.12.084.
- [45] P.A. Galione, C.D. Pérez-Segarra, I. Rodríguez, S. Torras, J. Rigola, Multi-layered solid-PCM thermocline thermal storage for CSP. Numerical evaluation of its

- application in a 50MWe plant, Sol. Energy 119 (2015) 134–150, https://doi.org/10.1016/j.solener.2015.06.029.
- [46] T. Roeder, K. Risthaus, N. Monnerie, C. Sattler, Non-stoichiometric redox thermochemical energy storage analysis for high temperature applications, Energies 15 (16) (2022) 5982, https://doi.org/10.3390/en15165982.
- [47] T. Schumann, Heat transfer: a liquid flowing through a porous prism, J. Franklin Inst. 208 (3) (1929) 405–416, https://doi.org/10.1016/S0016-0032(29)91186-8.
- [48] Z. Qi, A.B. Yu, A new correlation for heat transfer in particle-fluid beds, Int. J. Heat Mass Transf. 181 (2021) 121844, https://doi.org/10.1016/j. ijheatmasstransfer.2021.121844.
- [49] P. Stephan, S. Kabelac, M. Kind, D. Mewes, K. Schaber, and T. Wetzel, VDI-Wärmeatlas. Berlin, Heidelberg: Springer Berlin Heidelberg, 2019. 978-3-662-52988-1.
- [50] V. Gnielinski, Gleichungen zur Berechnung ses Wärme- und Stoffaustausches in durchströmten ruhenden Kugelschüttungen bei mittleren und großen Pecletzahlen, Verfahrenstechnik 12 (6) (1978) 363–366.
- [51] S. Ergun, Fluid flow through packed columns, Chem. Eng. Prog. 48 (2) (1952) 89-94.
- [52] F.P. Incropera, D.P. DeWitt, T.L. Bergman, A.S. Lavine, Fundamentals of heat and mass transfer, 6th ed., John Wiley & Sons, Hoboken, N. J, 2007.
- [53] P. Zehner, E.U. Schlünder, Wärmeleitfähigkeit von Schüttungen bei mäßigen Temperaturen, Chem. Ing. Tech. 42 (14) (1970) 933–941, https://doi.org/ 10.1002/cite.330421408.
- [54] P. Zehner, E.U. Schlünder, Einfluß der Wärmestrahlung und des Druckes auf den Wärmetransport in nicht durchströmten Schüttungen, Chem. Ing. Tech. 44 (23) (1972) 1303–1308, https://doi.org/10.1002/cite.330442305.
- [55] H.-J. Kretzschmar and W. Wagner, International Steam Tables: Properties of Water and Steam based on the Industrial Formulation IAPWS-IF97, 3rd ed. (Springer eBooks Engineering). Berlin, Heidelberg: Springer Vieweg, 2019. 9783662532195.
- [56] W. Wu, A centrifugal particle receiver for high-temperature solar applications, Logos-Verl, Berlin, 2015.
- [57] N. P. Siegel, M. D. Gross, and R. Coury, "The Development of Direct Absorption and Storage Media for Falling Particle Solar Central Receivers," *Journal of Solar Energy Engineering*, vol. 137, no. 4, 2015, Art. no. 041003, doi: 10.1115/1.4030069.
- [58] D.M. Amaya Dueñas, et al., Performance assessment of a 25 kW solid oxide cell module for hydrogen production and power generation, Int. J. Hydrogen Energy 59 (2024) 570–581, https://doi.org/10.1016/j.ijhydene.2024.01.346.
- [59] M. Cascetta, G. Cau, P. Puddu, F. Serra, Numerical investigation of a packed bed thermal energy storage system with different heat transfer fluids, Energy Procedia 45 (2014) 598–607, https://doi.org/10.1016/j.egypro.2014.01.064.
- [60] S. Zunft, M. Hänel, M. Krüger, V. Dreißigacker, A design study for regenerator-type heat storage in solar tower plants—results and conclusions of the HOTSPOT project, Energy Procedia 49 (2014) 1088–1096, https://doi.org/10.1016/j. egypro.2014.03.118.
- [61] Y. Kadohiro, et al., Cavity-shaped direct solar steam generator employing conical helical tube for high-temperature application: Model development, experimental testing and numerical analysis, Energy Convers. Manage.: X 18 (2023) 100366, https://doi.org/10.1016/j.ecmx.2023.100366.
- [62] D. Geldart, Types of gas fluidization, Powder Technol. 7 (5) (1973) 285–292, https://doi.org/10.1016/0032-5910(73)80037-3.
- [63] J. Grobbel, S. Brendelberger, M. Henninger, C. Sattler, R. Pitz-Paal, Calibration of parameters for DEM simulations of solar particle receivers by bulk experiments and surrogate functions, Powder Technol. 364 (2020) 831–844, https://doi.org/ 10.1016/j.powtec.2019.11.028.
- [64] T. Baumann, S. Zunft, Properties of granular materials as heat transfer and storage medium in CSP application, Sol. Energy Mater. Sol. Cells 143 (2015) 38–47, https://doi.org/10.1016/j.solmat.2015.06.037.
- [65] A. Meier, C. Winkler, D. Wuillemin, Experiment for modelling high temperature rock bed storage, Sol. Energy Mater. 24 (1–4) (1991) 255–264, https://doi.org/ 10.1016/0165-1633(91)90066-T.
- [66] "Superwool® Prime Blanket: Technisches Datenblatt," Morgan Advanced Materials, Sep. 2021.
- [67] S. Bell, Measurement Good Practice Guide No. 11 (Issue 2): The Beginner's Guide to Uncertainty of Measurement. Teddington, Middlesex, United Kingdom, TW11 0LW: National Physical Laboratory, 2001.
- [68] A. Weber, S. Schürg, T. Roeder, J. Grobbel, M.N. Puttkamer, C. Sattler, Experimental dataset of fluid flow and heat transfer in a shallow packed bed at low reynolds numbers, Data Brief (2025) 111743, https://doi.org/10.1016/j. dib.2025.111743.
- [69] V.K. Thanda, et al., Experimental investigation of the applicability of a 250 kW ceria receiver/reactor for solar thermochemical hydrogen generation, Renew. Energy 198 (2022) 389–398, https://doi.org/10.1016/j.renene.2022.08.010.
- [70] K. Wieghardt et al., "Synlight A new facility for large-scale testing in CSP and solar chemistry," in Santiago, Chile, 2018, p. 40042, doi: 10.1063/1.5067078.
- [71] D. Laaber, H. von Storch, K. Wieghardt, H. Fock, C. Sattler, and R. Pitz-Pahl, "One year with synlight Review of operating experience," in SOLARPACES 2018: International Conference on Concentrating Solar Power and Chemical Energy Systems, Casablanca, Morocco, 2019, p. 170007, doi: 10.1063/1.5117677.
- [72] T.R. Davenne, S.D. Garvey, B. Cardenas, J.P. Rouse, Stability of packed bed thermoclines, J. Storage Mater. 19 (2018) 192–200, https://doi.org/10.1016/j. est.2018.07.015.